

TECHNICAL REPORT BRL-TR-2987

BRL

AD-A206 748

STEADY FLOW COMBUSTION MODEL
FOR SOLID-FUEL RAMJET PROJECTILES

MICHAEL J. NUSCA

SDTIC
ELECTE
APR 10 1989
D^{cy}D

APRIL 1989

APPROVED FOR PUBLIC RELEASE; DISTRIBUTION UNLIMITED.

U.S. ARMY LABORATORY COMMAND

BALLISTIC RESEARCH LABORATORY
RDEN PROVING GROUND, MARYLAND

DESTRUCTION NOTICE

Destroy this report when it is no longer needed. DO NOT return it to the originator.

Additional copies of this report may be obtained from the National Technical Information Service, U.S. Department of Commerce, Springfield, VA 22161.

The findings of this report are not to be construed as an official Department of the Army position, unless so designated by other authorized documents.

The use of trade names or manufacturers' names in this report does not constitute indorsement of any commercial product.

REPORT DOCUMENTATION PAGE

Form Approved OMB No. 0704-0188

1a. REPORT SECURITY CLASSIFICATION UNCLASSIFIED		1b. RESTRICTIVE MARKINGS	
2a. SECURITY CLASSIFICATION AUTHORITY		3. DISTRIBUTION/AVAILABILITY OF REPORT Approved for public release; distribution is unlimited.	
2b. DECLASSIFICATION/DOWNGRADING SCHEDULE		5. MONITORING ORGANIZATION REPORT NUMBER(S)	
4. PERFORMING ORGANIZATION REPORT NUMBER(S) BRL-TR-2987		7a. NAME OF MONITORING ORGANIZATION	
6a. NAME OF PERFORMING ORGANIZATION U.S. Army Ballistic Research Laboratory	6b. OFFICE SYMBOL (if applicable) SLCBR-LF	7b. ADDRESS (City, State, and ZIP Code)	
8a. NAME OF FUNDING/SPONSORING ORGANIZATION U.S. Army Ballistic Research Laboratory		9. PROCUREMENT INSTRUMENT IDENTIFICATION NUMBER	
8b. OFFICE SYMBOL (if applicable) SLCBR-DD-T		10. SOURCE OF FUNDING NUMBERS	
8c. ADDRESS (City, State, and ZIP Code) Aberdeen Proving Ground, MD 21005-5066		PROGRAM ELEMENT NO. 62618A	PROJECT NO. 62618AH80
8d. ADDRESS (City, State, and ZIP Code) Aberdeen Proving Ground, MD 21005-5066		TASK NO.	WORK UNIT ACCESSION NO.
11. TITLE (Include Security Classification) Steady Flow Combustion Model for Solid-Fuel Ramjet Projectiles (U)			
12. PERSONAL AUTHOR(S) Nusca, Michael J.			
13a. TYPE OF REPORT Technical Report	13b. TIME COVERED FROM _____ TO _____	14. DATE OF REPORT (Year, Month, Day) 1989 January	15. PAGE COUNT 53
16. SUPPLEMENTARY NOTATION <i>continued from pg 1</i> <i>Keywords</i>			
17. COSATI CODES		18. SUBJECT TERMS (Continue on reverse if necessary and identify by block number)	
FIELD	GROUP	Solid-Fuel Ramjet;	
01	01	Combustion Model;	
21	08.2	Computational Fluid Dynamics	
19. ABSTRACT (Continue on reverse if necessary and identify by block number) The steady flow Navier-Stokes equations are written in stream function-vorticity form and solved using a Gauss-Seidel relaxation scheme. A diffusion-flame combustion model is formulated and linked to the Navier-Stokes equations by equations for the conservation of chemical species mass and source terms in the energy equation. Since a steady-state solution is produced, solid fuel ignition and depletion events are ignored. Radiation effects due to combustion are also neglected. The diffusion-flame combustion model assumes a mass-controlled reaction between fuel and oxidizer (air). The reaction occurs in one step and is unidirectional. The reaction is diffusion-controlled so that the reaction rate is faster than the diffusion rate. An actual value for the reaction rate is not required since a single equation for the conservation of fuel and oxidizer mass is formulated. The model includes the effects of axial rotation of the combustion chamber. A phenomenological turbulence model is used. Computed solid fuel regression rate and thrust for a solid-fuel ramjet projectile agree well with experimental data and in-flight observations.			
20. DISTRIBUTION/AVAILABILITY OF ABSTRACT <input type="checkbox"/> UNCLASSIFIED/UNLIMITED <input checked="" type="checkbox"/> SAME AS RPT. <input type="checkbox"/> DTIC USERS		21. ABSTRACT SECURITY CLASSIFICATION UNCLASSIFIED	
22a. NAME OF RESPONSIBLE INDIVIDUAL Michael J. Nusca		22b. TELEPHONE (Include Area Code) (301)-278-2057	22c. OFFICE SYMBOL SLCBR-LF-A

Table of Contents

	<u>Page</u>
List of Figures	v
I. INTRODUCTION	1
II. COMBUSTION MODEL	3
III. TURBULENCE MODEL	6
IV. BOUNDARY CONDITIONS	7
V. VALIDATION	8
1. Reattachment Length Data	9
2. Regression Rate Data	10
VI. RESULTS AND DISCUSSION	11
1. Inlet and Fueled-Wall Boundary Conditions	11
2. Computational Grid	12
3. Mean Flow Features	13
4. Combustion Flame	13
5. Flow Profiles	13
6. SFRJ Flight Performance	14
VII. CONCLUSIONS	15
REFERENCES	35
APPENDIX A	37
APPENDIX B	43
LIST OF SYMBOLS	49
DISTRIBUTION LIST	51

DTIC

Accession for	
NTIS CRA&I	<input checked="" type="checkbox"/>
DTIC TAB	<input type="checkbox"/>
Unannounced	<input type="checkbox"/>
Justification _____	
By _____	
Distribution [_____]	
Availability Codes	
Dist	Availability for _____
A-1	

List of Figures

<u>Figure</u>		<u>Page</u>
1	SFRJ Geometry; Dimensions in Millimeters, $D_{inj} = 43.2$ mm, $D_{nt} = 40.6$ mm. (I) Inlet, (II) Injector, (III) Combustion Chamber, (IV) Fueled Wall, (V) Nozzle.	17
2	Schematic of Steady-State Combustion in the Chamber of an SFRJ.	18
3	Variation of Laminar Reattachment Length with Reynolds Number, Inert Flow, $Re = 40$ to 200	19
4	Variation of Reattachment Length with Spinrate, Inert Flow, $Re = 31000$	20
5	Regression Rate Distribution Along the Fueled Wall of a SFRJ; Connected-Pipe Test.	21
6	Variation of Regression Rate with Mass Flow Rate in a SFRJ; Connected-Pipe Test.	22
7	Computed Velocity Vectors for the Flowfield Near the Injector of a SFRJ.	23
8	Computed Velocity Vectors for the Flowfield Near the Nozzle of a SFRJ.	24
9	Computed Temperature Contours.	25
10	Computed Streamwise Velocity Profiles.	26
11	Computed Mass Fraction Profiles; $X = 0.136$ inches.	27
12	Computed Mass Fraction Profiles; $X = 2.038$ inches.	28
13	Computed Mass Fraction Profiles; $X = 5.942$ inches.	29
14	Computed Temperature Profiles.	30
15	Computed Density Profiles.	31
16	Velocity-Time History of Fin-Stabilized SFRJ Round 26362.	32
17	Drag Coefficient vs. Mach Number for Fin-Stabilized SFRJ Round 26362.	32
18	Thrust vs. Time for Fin-Stabilized SFRJ Round 26362; Measured and Computed.	33
B1	Portion of the Computational Grid. Solid circles are grid points. Open circles are cell centroids. Dotted lines enclose the rectangular area of integration.	48

I. INTRODUCTION

Various solid-fuel ramjet (SFRJ) tubular projectiles have been developed by the U.S. Army Ballistic Research Laboratory (BRL).^{1,2} One of these projectiles, a spin-stabilized 75mm version (see Figure 1), has been designed for use as a tank gun training round (TGTR) for the 105mm, M68 tank cannon. The goal of this development is to demonstrate a TGTR of low dispersion at three kilometers and with a maximum (safety) range of eight kilometers. The concept of the TGTR is to use the thrust (hence low drag) of the SFRJ projectile to obtain a ballistic match with low drag kinetic energy projectiles up to three kilometers. Upon depletion of the propellant and choking of the internal flow, the SFRJ will become a high-drag projectile with limited range. The 40mm version of the SFRJ projectile has also been tested.³ The flight characteristics of these projectiles were studied in both free flight, using radar, and flight thru an instrumented ballistic range.

In order to investigate the internal flow in an SFRJ, several wind tunnel tests were conducted by the BRL, Launch and Flight Division using unfueled, non-spinning, full-scale models.⁴ These tests provided internal surface pressure measurements for a variety of configurations at a freestream Mach number of 4.03. Both choked (subsonic internal flow) and unchoked (supersonic internal flow) cases were studied. Subsequently, Nusca, Chakravarthy, and Goldberg⁵ used a zonal computational fluid dynamics (CFD) code to compute the internal flowfield (choked and unchoked flow) for several 75mm SFRJ internal configurations. These computed results were for unreacting flow and were compared with measured internal wall pressure data. In addition, CFD has been applied to the 40mm SFRJ projectile.³

Computational efforts aimed at modeling the combustion in the SFRJ are essential to future design modifications and applications of the SFRJ to high-velocity, low drag, anti-tank projectile systems. Vos^{6,7} has developed a finite chemical kinetics, multistep, combustion model combined with a solution algorithm for parabolic and elliptic partial differential equations (subsonic flow). Models of this type are candidates for use in zonal CFD codes. This model has been applied to a combustion chamber similar to that of the SFRJ. Instead of solid fuel, however, Vos considered the injection of hydrogen gas (H_2) into an oxygen (O_2) stream. Reported comparisons of this multistep model to a simple one-step diffusion flame model⁷ demonstrated that even the more basic approach provides an adequate simulation of a reacting flow.

¹ Mermagen W.H., and Yalamanchili R.J., "First Diagnostic Tests of a 75mm Solid Fuel Ramjet Tubular Projectile," ARBRL-MR-03283, U.S. Army Ballistic Research Laboratory, Aberdeen Proving Ground, MD, June 1983. (AD A130598)

² Mermagen W.H., and Yalamanchili R.J., "Experimental Tests of a 105/75mm Solid Fuel Ramjet Tubular Projectile," ARBRL-MR-3416, U.S. Army Ballistic Research Laboratory, Aberdeen Proving Ground, MD, December 1984. (AD B089766)

³ Nusca, M.J., and Oskay, V.O., "Comparison of Computational Analysis with Flight Tests of a 40mm Solid-Fuel Ramjet Projectile," U.S. Army Ballistic Research Laboratory, Aberdeen Proving Ground, MD, Technical Report in publication.

⁴ Kayser L.D., Yalamanchili R.J., and Trezler C., "Pressure Measurements on the Interior Surface of a 75mm Tubular Projectile at Mach 4," ARBRL-MR-3725, U.S. Army Ballistic Research Laboratory, Aberdeen Proving Ground, MD, December 1988.

⁵ Nusca, M.J., Chakravarthy, S.R., and Goldberg, U.C., "Computational Capability for the Solid Fuel Ramjet Projectile," ARBRL-TR-2958, U.S. Army Ballistic Research Laboratory, Aberdeen Proving Ground, MD, December, 1988.

⁶ Vos, J.B., "Calculating Turbulent Reacting Flows Using Finite Chemical Kinetics," *AIAA Journal*, Vol. 25, No. 10, October 1987, pp. 1965-1972.

⁷ Vos, J.B., "The Calculation of Turbulent Reacting Flows with a Combustion Model Based on Finite Chemical Kinetics," Ph.D. Dissertation, Dept. of Aerospace Engineering, Delft University, the Netherlands, 1987.

Gielda⁸ employed a time-accurate MacCormack predictor-corrector scheme to solve the unsteady, axisymmetric Navier-Stokes equations with five additional species continuity equations. The code was implemented on a CRAY X-MP/48 computer and required 3 to 6 CPU hours per solution. The assumptions made in this code include supersonic inflow and outflow boundary conditions (i.e. no thermal choking and an oblique leading edge shock) and a prescribed solid fuel regression rate (.11 cm/sec) and fuel surface temperature (2000 R). The prescribed regression rate is used to determine a constant injection velocity that is applied to the fueled wall surface. A turbulence model is not employed. Results for inert flow as well as flow with solid fuel decomposition and gas phase combustion are achieved. The application of this model to the ramjet projectile is unclear for two reasons. First, the combustion chamber of a ramjet requires an inlet flow Mach number of about .2 to .3. Deceleration of the supersonic freestream, in the diffuser, may be caused by a leading-edge normal shock.⁹ The SFRJ projectile is choked (i.e. expelled leading-edge normal shock) when combustion is occurring in flight, as observed in shadowgraphs taken during range testing.³ Thus a supersonic inflow boundary condition for the combustion chamber, when combustion is occurring, is not justifiable. Secondly, specification of an injection velocity at the fueled wall precludes the use of measured fuel regression rates for code validation.

The present steady-state combustion model assumes a heterogeneous mass-controlled reaction between solid fuel (bound to the lateral wall of the combustion chamber) and an incoming subsonic airstream. Figure 2 summarizes the main features of steady-state combustion in the SFRJ. Because the solution is for steady-state, solid fuel ignition and depletion events are ignored. The reaction between fuel and oxidizer (air) yields products that are considered a single specie. The reaction occurs in one step and is irreversible. Fuel and air are fully consumed in the reaction, and they may not coexist at any point in the flowfield. In addition, the reaction is diffusion controlled such that the reaction rate is much faster than the rate of diffusion. This diffusion-flame combustion model is incorporated into the overall flow solution by source terms in the Navier-Stokes equations and equations for the conservation of chemical species mass. Radiation effects due to combustion are neglected. The model includes the effect of axial rotation of the chamber. Studies on this and similar models for combustion chamber flows have been performed.¹⁰⁻¹⁶ Diffusion-flame models have been demonstrated to be as valid for SFRJ simulations as models with finite-rate kinetics.¹⁶ However, finite-rate kinetics combustion models require numerical values of the reaction rates for all species. These rates are not readily available for complex solid fuels, especially those with oxidizer additives.

⁸ Gielda, T.P., "Numerical Simulation of Chemically Reacting Solid Fuel Ramjet Internal Flowfields," Final Report for U.S. Army Ballistic Research Laboratory Contract No. DAAL03-86-D-0001, February 1988.

⁹ Hill, P. and Peterson, C., *Mechanics and Thermodynamics of Propulsion*, Addison-Wesley, 1965.

¹⁰ Khalil, E.E., Spalding, D.B., and Whitelaw, J.H., "The Calculation of Local Flow Properties in Two-Dimensional Furnaces," *International Journal of Heat and Mass Transfer*, 1975, Vol. 18, pp. 775-791.

¹¹ Bradshaw, P., Cebeci, T., and Whitelaw, J.H., *Engineering Calculation Methods for Turbulent Flows*, Academic Press, New York, 1981.

¹² Kuo, K.K., *Principles of Combustion*, John Wiley and Sons, Inc., New York, 1986.

¹³ Williams, F.A., *Combustion Theory*, Addison-Wesley Publishing Company, Inc., 1965.

¹⁴ Vanka, S.P., "Calculation of Axisymmetric, Turbulent, Confined Diffusion Flames," *AIAA Journal*, Vol. 24, No. 3, March 1986, pp. 462-469.

¹⁵ Kim, Y.M., and Chung, T.J., "Finite Element Analysis of Turbulent Diffusion Flames," AIAA-88-0062, Proceedings of the 26th AIAA Aerospace Sciences Meeting, January 11-14, 1988, Reno, NV.

¹⁶ Elands, P.J.M., Korting, P.A.O.G., Dijkstra, F., and Wijchers, T., "Combustion of Polyethylene in a Solid Fuel Ramjet - A Comparison of Computational and Experimental Results," AIAA-88-3043, Proceedings of the 26th AIAA Aerospace Sciences Meeting, January 11-14, 1988, Reno, NV.

For the present study a Gauss-Seidel relaxation scheme was applied to the steady flow Navier-Stokes equations with the local flow velocity constrained to be smaller than the local speed of sound (i.e. Mach number < 1). Thus the governing equations are elliptic. The stream-function (ψ) and vorticity (ω) form of the equations was used. In order to clearly examine methods of incorporating the effects of solid fuel combustion in CFD codes, the present subsonic flow code was chosen over the general flow code described in Reference 5. The present combustion model can be used with more sophisticated CFD codes, and a wider range of flow conditions can be investigated. The present code requires from 0.5 to 1.0 CPU hours per solution (inert and reacting flow, respectively) on a CRAY X-MP/48 computer. The code is therefore suitable for SFRJ combustor design studies.

The governing equations are derived in Appendix A. The combustion model, turbulence model, and boundary conditions are described in the following sections. The solution scheme is described in Appendix B.

II. COMBUSTION MODEL

Figure 2 shows the assumed major features of steady-state combustion in the SFRJ. Most of these features have been measured or inferred from connected-pipe tests.¹⁷ Behind the injector a region of recirculating flow is formed. This region serves to bring oxidizer from the inlet to the solid fuel surface. The flame originates from this region, and thus the recirculating flow acts as a flameholder. Tests have shown that combustion is not sustained without this flow.¹⁷ The flame may or may not reach the centerline of the combustion chamber at the exit plane. If it does not, gas between the centerline and the leading edge of the flame consists of air and products that have been accelerated to a velocity above the inlet value (assumed to be smaller than the local sound speed). Between the flame and the combustor wall, the gas consists of fuel and products. The forward-facing step, at the nozzle entrance, retards the flow, but the flow does not separate.

Systems of chemical reactions are usually complex. A hydrocarbon fuel, for example, may contain hundreds of distinct chemical species. During combustion, numerous short-lived intermediate species are formed in addition to the final products that include H_2O , CO , and CO_2 . Even if it were technically desirable and computationally possible to include all these species and reactions within the framework of a calculation, to attempt to do so would be defeated by an ignorance of the thermodynamic, transport, and chemical-kinetic properties of the great majority of the species. It is possible to make useful predictions of combustion processes by confining attention to an idealized reaction between fuel and oxidizer, neglecting intermediate compounds and considering simple reactions when fuel and oxidizer combine in a fixed mass ratio.

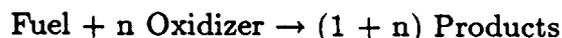
Many of the assumptions commonly made in combustion models^{12,13} are also incorporated into the present model. In particular, assumptions made in the Shvab-Zeldovich formulation.¹³ The reacting fluid is treated as a continuum with equal mass diffusivity

¹⁷ MaClaren, R.O., and Holzman, A.L., "SFRJ Projectile Development," Final Report, CSD-2710-FR, United Technologies Chemical Systems Division, Sunnyvale, CA., 26 June 1981. (See also, Hussain, S.M., and Holzman, A.L., "Effects of Spin on SFRJ Projectile Performance," Monthly Progress Report No. 12, Contract No. DAAA15-86-C-0008, 1 Dec - 31 Dec., 1986.)

(Γ_j) properties for all species. The specific heat at constant pressure (c_p) of each species is assumed constant in the gas phase. Combustion-generated turbulence, the turbulence generated in addition to that of the isothermal flow, is included by using a phenomenological, one-equation model (see Section III). The reacting solid surface is considered energetically homogeneous (i.e. gas-solid interface effects are neglected). Radiation energy transfer is assumed to be negligible. A one-step, mass-controlled reaction is assumed for which the reactant species are fully consumed. The reaction flame is considered to be nonpremixed, steady, nearly isobaric, and of zero thickness, i.e. a diffusion flame.¹³

The concept of the diffusion flame differs from that of a premixed flame in which reactants are perfectly mixed prior to chemical reaction.¹² Since the solid fuel is bound to the combustor wall and ablates into the airstream to react with oxidant, the diffusion flame model more closely matches the physical environment of the SFRJ. However, the difficulty in modeling reacting turbulent flows with nonpremixed reactants lies in the handling of the mean chemical production terms.¹²

Consider an irreversible, one-step chemical reaction between fuel and oxidizer. The reaction maintains a fixed stoichiometric ratio, and the reaction rate is much faster than the rate of diffusion so that the reaction is diffusion controlled.¹¹ The products of combustion are treated as a single species.



Conservation of chemical species (Equation A24) can be written for each specie in the above reaction. In particular, the mass conservation of fuel and oxidizer are expressed as:

$$\frac{\partial}{\partial z} \left[m_{\text{fu}} \frac{\partial \psi}{\partial r} \right] - \frac{\partial}{\partial r} \left[m_{\text{fu}} \frac{\partial \psi}{\partial z} \right] - \frac{\partial}{\partial z} \left[(\Gamma_{\text{fu}})_{\text{eff}} r \frac{\partial m_{\text{fu}}}{\partial z} \right] - \frac{\partial}{\partial r} \left[(\Gamma_{\text{fu}})_{\text{eff}} r \frac{\partial m_{\text{fu}}}{\partial r} \right] - r R_{\text{fu}} = 0 \quad (1)$$

$$\frac{\partial}{\partial z} \left[m_{\text{ox}} \frac{\partial \psi}{\partial r} \right] - \frac{\partial}{\partial r} \left[m_{\text{ox}} \frac{\partial \psi}{\partial z} \right] - \frac{\partial}{\partial z} \left[(\Gamma_{\text{ox}})_{\text{eff}} r \frac{\partial m_{\text{ox}}}{\partial z} \right] - \frac{\partial}{\partial r} \left[(\Gamma_{\text{ox}})_{\text{eff}} r \frac{\partial m_{\text{ox}}}{\partial r} \right] - r R_{\text{ox}} = 0 \quad (2)$$

Where R_{fu} and R_{ox} are the reaction rates per unit volume and m is a mass fraction. For a general multi-step reaction, these reaction rates are difficult to accurately measure. Indeed, the uncertainty of these data for combustion models places a severe restriction on the accuracy of the entire computation. However, for the one-step reaction described above, the reaction rate of fuel (R_{fu}) and oxidizer (R_{ox}) are negative (since these reactants are consumed), and are related by;

$$\begin{aligned} R_{\text{fu}} &= R_{\text{ox}}/n \\ R_{\text{fu}} &= -R_{\text{pr}}/(1 + n) \\ R_{\text{ox}}/n &= -R_{\text{pr}}/(1 + n) \end{aligned}$$

The R terms can be eliminated from Equations 1 and 2 by dividing Equation 2 by n and subtracting the resultant equation from Equation 1:

$$\begin{aligned}
\frac{\partial}{\partial z} \left[\left(m_{fu} - \frac{m_{ox}}{n} \right) \frac{\partial \psi}{\partial r} \right] - \frac{\partial}{\partial r} \left[\left(m_{fu} - \frac{m_{ox}}{n} \right) \frac{\partial \psi}{\partial z} \right] \\
- \frac{\partial}{\partial z} \left[r \left((\Gamma_{fu})_{eff} \frac{\partial m_{fu}}{\partial z} - (\Gamma_{ox})_{eff} \frac{\partial m_{ox}/n}{\partial z} \right) \right] \\
- \frac{\partial}{\partial r} \left[r \left((\Gamma_{fu})_{eff} \frac{\partial m_{fu}}{\partial r} - (\Gamma_{ox})_{eff} \frac{\partial m_{ox}/n}{\partial r} \right) \right] = 0 \quad (3)
\end{aligned}$$

Assuming that fuel and oxidizer have identical diffusion properties (i.e. that the diffusion coefficients, $\Gamma_j = \mu_{eff}/\text{Schmidt Number}$, are equal), then $\Gamma_{fu} = \Gamma_{ox} \equiv \Gamma_{fo}$. Equation 3 can be written in terms of $\phi_{fo} \equiv m_{fu} - m_{ox}/n$ as,

$$\frac{\partial}{\partial z} \left[\phi_{fo} \frac{\partial \psi}{\partial r} \right] - \frac{\partial}{\partial r} \left[\phi_{fo} \frac{\partial \psi}{\partial z} \right] - \frac{\partial}{\partial z} \left[r (\Gamma_{fo})_{eff} \frac{\partial \phi_{fo}}{\partial z} \right] - \frac{\partial}{\partial r} \left[r (\Gamma_{fo})_{eff} \frac{\partial \phi_{fo}}{\partial r} \right] = 0 \quad (4)$$

Assuming that $\Gamma_{fu} = \Gamma_{pr} \equiv \Gamma_{fp}$ and $\Gamma_{ox} = \Gamma_{pr} \equiv \Gamma_{op}$, then Equation 4 can be written in terms of $\phi_{fp} \equiv m_{fu} + m_{pr}/(1+n)$ or $\phi_{op} \equiv m_{ox}/n + m_{pr}/(1+n)$, as well.

In terms of the general form of the conservation equations (Equation A25), the equation for $\phi = m_j$ is replaced with three equations, where:

$$\begin{array}{llllll}
\phi = \phi_{fo} = m_{fu} - m_{ox}/n, & a_\phi = 1, & b_\phi = (\Gamma_{fo})_{eff}, & c_\phi = 1, & d_\phi = 0 \\
\phi = \phi_{fp} = m_{fu} + m_{pr}/(1+n), & a_\phi = 1, & b_\phi = (\Gamma_{fp})_{eff}, & c_\phi = 1, & d_\phi = 0 \\
\phi = \phi_{op} = m_{ox}/n + m_{pr}/(1+n), & a_\phi = 1, & b_\phi = (\Gamma_{op})_{eff}, & c_\phi = 1, & d_\phi = 0
\end{array}$$

Mixture fractions (f_{fo} , f_{fp} , and f_{op}) are formed from linear combinations of the conserved variables (ϕ_{fo} , ϕ_{fp} , and ϕ_{op}) and are thus conserved variables as well.

$$f_{fo} = \frac{\phi_{fo} - (\phi_{fo})_{ox}}{(\phi_{fo})_{fu} - (\phi_{fo})_{ox}} = \frac{\phi_{fo} + 1/n}{1 + 1/n} = \left(\frac{n}{1+n} \right) \phi_{fo} + \left(\frac{1}{1+n} \right) \quad (5)$$

$$f_{fp} = \frac{\phi_{fp} - (\phi_{fp})_{pr}}{(\phi_{fp})_{fu} - (\phi_{fp})_{pr}} = \frac{\phi_{fp} - 1/(1+n)}{1 - 1/(1+n)} = \left(\frac{1+n}{n} \right) \phi_{fp} - \left(\frac{1}{n} \right) \quad (6)$$

$$f_{op} = \frac{\phi_{op} - (\phi_{op})_{pr}}{(\phi_{op})_{ox} - (\phi_{op})_{pr}} = \frac{\phi_{op} - 1/(1+n)}{1/n - 1/(1+n)} = (n + n^2) \phi_{op} - n \quad (7)$$

At the stoichiometric air/fuel ratio ($m_{ox}/m_{fu} = n$), fuel and oxidizer are consumed ($m_{fu} = m_{ox} = 0$) and products are formed ($m_{pr} = 1$), thus the mixture fractions are:

$$(\phi_{fo})_{st} = 0, \quad (\phi_{fp})_{st} = \frac{1}{1+n}, \quad (\phi_{op})_{st} = \frac{1}{1+n}, \quad (8)$$

$$(f_{fo})_{st} = \frac{1}{1+n}, \quad (f_{fp})_{st} = 0, \quad (f_{op})_{st} = 0 \quad (9)$$

The flame location is indicated by the flow contour along which $f_{fo} = 1/(1+n)$ and $m_{pr} = 1$. At this location both the maximum flow temperature and a reduction in local flow density occur.¹⁰ The mass fractions (m_{fu} , m_{ox} , m_{pr}) are decoded from the mixture fractions by

assuming that fuel and air are completely consumed in the reaction and both fuel and air cannot coexist at any point in the flowfield. Thus,

$$\begin{aligned} 0 \leq f_{fo} \leq (f_{fo})_{st} & : m_{fu} = 0, \quad m_{ox} = 1 - (1+n)f_{fo}, \quad m_{pr} = 1 - m_{ox} \\ (f_{fo})_{st} \leq f_{fo} \leq 1 & : m_{ox} = 0, \quad m_{fu} = \left(\frac{n+1}{n}\right)f_{fo} - \left(\frac{1}{n}\right), \quad m_{pr} = 1 - m_{fu} \end{aligned}$$

In summary, the present combustion model assumes a mass-controlled reaction between fuel and oxidizer, yielding reaction products that are treated as a single specie. Fuel and air may not coexist at any point in the flowfield. The reaction occurs in one step and is irreversible. The reaction rates are much faster than the rate of diffusion, i.e. diffusion controlled reaction. The requirement of actual values of the reaction rates has been eliminated by using a single equation for the conservation of combined fuel and oxidizer mass (Equation 3). Radiation effects due to combustion are ignored. Solid fuel ignition and depletion events are not treated since steady flow is assumed.

III. TURBULENCE MODEL

Modeling the effective viscosity, $\mu_{eff} = \mu + \mu_t$, for a turbulent, reacting flow has been the subject of much investigation.^{12,13,18} For some limited applications, the turbulent kinetic energy and dissipation rate model, or $k - \epsilon$ model, has been shown to be applicable to the reacting flow in a combustion chamber.¹⁰ The turbulent viscosity is defined as:

$$\mu_t = C_\mu \rho k^2 / \epsilon = \mu_{eff} - \mu \quad (10)$$

where C_μ is a function of the turbulent Reynolds number, $Re_t = \rho k^{1/2} l / \mu$, with l defined as the turbulence length scale. The governing equations for k and ϵ can be written in the form of Equation A25, with:

$$\begin{aligned} \phi = k, & \quad a_\phi = 1, & \quad b_\phi = (\Gamma_k)_{eff}, & \quad c_\phi = 1, & \quad d_\phi = -S_k \\ \phi = \epsilon, & \quad a_\phi = 1, & \quad b_\phi = (\Gamma_\epsilon)_{eff}, & \quad c_\phi = 1, & \quad d_\phi = -S_\epsilon \end{aligned}$$

where the diffusion coefficients for k and ϵ are defined as μ_{eff} /Schmidt Number. Equation 10 implies an isotropic turbulent viscosity (homogeneous flow without mean velocity variations).¹⁰ With diffusion and dissipation terms in the equations for turbulent kinetic energy and dissipation rate, the isotropic assumption represents a limitation on the accuracy of flow calculations, even without combustion. For example, normal stresses may vary considerably throughout the flowfield. These variations, and any implication that they may have for the values of mean velocity, will not be represented by this turbulence model. In addition, the model has been shown to yield good predictions in a wide range of boundary layer flows, but only limited testing has been attempted in subsonic flows with recirculation and swirl. For flows with combustion, the difficulty lies in an adequate formulation for the source terms S_k and S_ϵ .¹⁰

¹⁸ Ballal, D.R., "Combustion-Generated Turbulence in Practical Combustors," *AIAA Journal of Propulsion*, Vol. 4, No. 5, Sept-Oct 1988, pp. 985-990.

Combustion-generated turbulence, the turbulence generated in addition to that of the isothermal flow, has been widely investigated using experimental procedures. For enclosed air-fuel mixing/reaction chambers, the available data has been summarized by Ballal.¹⁸ Combustion-generated turbulence is strongly affected by flow density, pressure and temperature gradients, inlet blockage ratio (step height of the flameholder and the size of the subsequent flow recirculation zone), inlet flow momentum, and flow swirl (combustion chamber rotation). Experiments in these combustors have revealed that, relative to the isothermal flow, the combustion process increases the strength and decreases the size of the flow recirculation zone behind the inlet step. As the size of the recirculation zone decreases, combustion-generated turbulence increases sharply. Swirl is commonly employed in combustors to improve flame stability and fuel-air mixing and to shorten the flame length. Experimental evidence shows that combustion-generated turbulence rapidly increases with flow swirl. Many of these effects can be included in phenomenological models that correlate well with available data.

A phenomenological model for the effective viscosity in a confined, turbulent, steady diffusion flame was proposed by Pun and Spalding:^{19,20}

$$\mu_{\text{eff}} = KD^{2/3}L^{-1/3}\rho^{2/3}\left(\dot{m}u^2 + \dot{m}(rv)^2\right)_{\text{inlet}}^{1/3} \quad (11)$$

where K is a constant and is chosen to insure that the proper value of μ_{eff} is prescribed at the inlet. The parameters D and L are the maximum diameter and length of the combustion chamber, respectively. The inlet axial and azimuthal velocity are denoted u and v , respectively. The inlet swirl velocity is rv . This model assumes that μ_{eff} increases with ρ , D , and the momentum (or kinetic energy) of the fluid entering the chamber (including flow swirl), but decreases with increasing chamber length, L . This model has been studied for simulation of steady, confined, turbulent flames.²⁰

IV. BOUNDARY CONDITIONS

For an SFRJ, the present combustion model considers only the flow within the fueled combustion chamber. The boundaries of this chamber are the inlet at the injector, the exit at the nozzle throat, the symmetry axis about which the chamber may rotate, and the solid wall (Figure 2). Since the governing equations (Equation A25) are elliptic, the conditions along these boundaries must prescribe values of the dependent variables, the gradient of the dependent variables in the normal direction, or an algebraic relation which connects the values of the dependent variables to the normal component of velocity. The sensitivity of the flow solution to the boundary conditions has been examined.

At the inlet plane, radial profiles of all dependent variables — ψ, ω, m_j or f, \tilde{h} , and v , — as well as values for T, p, ρ , and μ_{eff} are specified. For combustion chamber flows, the sensitivity of the flow solution to the shape of the initial velocity and temperature profiles

¹⁹ Pun, W.M., and Spalding, D.B., "A Procedure for Predicting the Velocity and Temperature Distributions in a Confined, Steady, Turbulent, Gaseous, Diffusion Flame," Imperial College, Mechanical Engineering Department Report SF/TN/11, 1967.

²⁰ Patankar, S.V., and Spalding, D.B., "A Computer Model for Three-Dimensional Flow in Furnaces," Proceedings of the 14th International Symposium on Combustion, Pennsylvania State University, August 20-25, 1972, pp.605-614.

has been found to be insignificant.¹⁰ It is assumed that the flow at the inlet plane consists of air ($f_{fo} = 0$, $f_{fp} = -1/n$, $f_{op} = 1$) and that the combustion process does not effect the inlet flow. In addition, a subsonic inlet flow assumption is used in accordance with the elliptic nature of the governing equations. These assumptions are not unreasonable for the SFRJ projectile. The solid-fuel ramjet projectile is designed for subsonic combustion¹⁷ and only limited evidence for the leakage of combustion products forward of the injector has been observed.² Hence, elliptic solvers can be used.

The exit plane is located at the nozzle throat where the flow is assumed to be subsonic. The streamlines at the exit plane are assumed to be parallel to the symmetry axis; thus flow gradients along the streamlines are zero. These assumptions are reasonable since experience for large Reynolds numbers has shown that the exact nature of the exit plane boundary conditions has little effect on the flowfield solution when convection is significant (i.e. large inlet mass flow).¹⁰

For mass continuity, the symmetry axis is considered to be a streamline of the flow, thus $\psi = \text{constant}$. Along the symmetry axis $r = 0$, thus $\partial\psi/\partial z = \partial\psi/\partial r = 0$ via Equations A1 and A2. The value of ψ along this boundary can be determined from values of ψ adjacent to the boundary using a one-sided finite difference for $\partial\psi/\partial r$ at the axis. From Equation A3, the boundary value for ω is zero. The axis boundary values for the remaining dependent variables, ϕ , are determined from $\partial\phi/\partial r = 0$.

The no-slip condition ($u = w = 0$, and $v/r = \Omega$, where Ω is the wall spinrate) is applied to the solid walls. Therefore $\psi = \text{constant}$, via Equations A1 and A2. For convenience $\psi = 0$ is chosen. One-sided finite differences for $\partial\psi/\partial r$ and $\partial\psi/\partial z$ are used in Equation A3 to determine the wall value for ω . For an inert wall (unfueled), the normal gradient of all mixture fractions, $\partial f/\partial n$, are set to zero. For a fueled wall, the boundary condition is based on the assumption that the wall is a source of fuel ($f_{fo} = 1$, $f_{fp} = 1$, $f_{op} = -n$). The wall temperature is set to the vaporization temperature of the fuel, $T_{\text{wall}} = T_{\text{vap}}$. The rate of burning (regression rate) on the fueled wall varies as a function of position along the wall and is determined from the temperature gradient normal to the wall,¹⁶

$$\dot{r} = \frac{q_{\text{wall}}}{\rho_{\text{wall}} h_v} \quad (12)$$

where q_{wall} is the local heat flux to the wall ($-\kappa\partial T/\partial r)_{\text{wall}}$, ρ_{wall} is the density of the fueled wall, and h_v is the heat of vaporization of a unit mass of solid fuel. Values of the thermal conductivity (κ), density, and heat of vaporization can be determined for most solid fuels.

V. VALIDATION

The present steady-state, elliptic flow solver and combustion model can be validated using available data for ramjet-type configurations (e.g. sudden-expansion combustors). Detailed experimental data for reacting internal flows in these configurations are rare, and the current simulation is aimed at overall flow properties. Comparison with measured data focuses on three features: injector flows, fuel regression rate, and thrust.

The rearward-facing step at the inlet (i.e. the injector) is required to initiate and

sustain the combustion flame in an SFRJ.¹⁷ Within this zone, air is mixed with fuel, and the solid-fuel regression rate is a maximum. Therefore, proper simulation of the flow reattachment point on the fueled wall is essential.

The solid fuel regression rate (\dot{r}) in SFRJ combustors has been measured using several methods. Equation 12 indicates that \dot{r} is proportional to the temperature gradient normal to the fueled wall. Accurate simulation of this quantity is essential to SFRJ design studies where the fuel burn time must be selected to achieve required flight characteristics.

Prediction of the thrust generated by a SFRJ is also essential to design studies and will be addressed in Section VI.6.

1. Reattachment Length Data

Lee²¹ conducted a computational study of recirculating laminar and turbulent flows through an abrupt pipe expansion. The flow was chemically inert. This study employed the stream function-vorticity equations in finite difference form and a $k-\epsilon$ model for turbulence closure. A Gauss-Seidel solution scheme was used. Results were generated for a variety of inlet flow profiles including uniform or plug flow and fully developed flow. Flow Reynolds numbers (based on the inlet pipe diameter), ranged from 10 to 200 for laminar boundary layers and 1000 to 1 million for turbulent flows. The ratio of internal pipe diameter to inlet diameter was 2 (step height equivalent to 25% of the combustor diameter). Comparison with experimental data from several sources was used to validate the code. The present code, without combustion model, was compared to Lee's calculations of flow reattachment length for laminar Reynolds numbers and uniform inlet flow. Turbulent calculations were not compared since a $k-\epsilon$ turbulence model was not employed in the present code. Figure 3 shows a nearly linear variation of reattachment length with Reynolds number. Agreement between two independent calculations is good.

So and Ahmed²² conducted an experimental investigation of inert flow in a sudden-expansion combustor. Low speed flow (13.1 ft/sec) in a long tube with a well contoured inlet and nozzle was measured with a laser-Doppler velocimeter (LDV) for various values of combustor axial spinrate. The ratio of combustor diameter to inlet diameter (at the end of the inlet nozzle) was 1.5 (step height equivalent to 16% of the combustor diameter). At the entrance to the combustor, the flow had been accelerated to 34.8 ft/sec. The Reynolds number based on this velocity and the inlet diameter was 31,000. Figure 4 indicates that the flow recirculation zone is compressed by combustor spin. The flow reattachment length (measured from the step) is normalized by the step height above the combustor wall. Comparison of this data with results from the present code are also shown. While the zero spin value is reproduced by the present code, calculations show that the variation with spinrate is less significant than indicated by the data.

²¹ Lee, J.J., "Heat and Mass Transfer Calculations for Recirculating Laminar and Turbulent Flows in an Abrupt Pipe Expansion," AIAA-88-3791, Proceedings of the 1st AIAA/ASME/SIAM/APS National Fluid Dynamics Congress, July 25-28, 1988, Cincinnati, OH.

²² So, R.M.C., and Ahmed, S.A., "Rotation Effects on Axisymmetric Sudden-Expansion Flows," AIAA Journal of Propulsion and Power, Vol. 4, No. 3, May-June 1988, pp. 270-276.

2. Regression Rate Data

Holzman and Husian¹⁷ at United Technologies Chemical Systems Division (UTC-CSD) have measured the solid fuel regression rate in an SFRJ using a connected-pipe test stand. The internal geometry of the model closely resembled that of the 75mm SFRJ (Figure 1). The solid fuel used in the tests was the same as that used in the SFRJ projectile. A typical inlet mass flux for the tests was 1814 grams/sec (4 lb/sec) at an inlet velocity of approximately 9.1 m/sec (30 ft/sec) and a temperature of 1840 R. The ratio of the combustor diameter to the inlet diameter was 1.42 (step height equivalent to 15% of the combustor diameter). Measurements were taken for combustor axial spinrates from 0 to 35,000 rpm (3665 rad/sec). The solid fuel regression rate was determined from the measured fuel grain regression and the test run time.

The solid fuel consists of four main components: 30% ammonium perchloride (NH_4ClO_4), 28.5% hydroxyl-terminated polybutadiene ($\text{C}_4\text{H}_{8.052}\text{O}_{0.005}$), 40% Escorez ($\text{C}_{7.398}\text{H}_{11.059}$), and 1.5% Catocene ($\text{C}_{27}\text{H}_{32}\text{Fe}_2$). The main products of combustion are hydrocarbon, oxygen, water and nitrogen.²³ For this study the assumed products are 67% CH_2 , 16.3% O_2 , 12.1% H_2O , and 4.9% N_2 . Thus, the molecular weights of the fuel, oxidizer and products are 97.7, 28.8, and 18.2 grams/mole, respectively. The fuel density, heat of vaporization, vaporization temperature, and stoichiometric air/fuel ratio are 1.189 grams/cc (74.2 lb/ft³), 2.8998×10^7 Joules/kg (12465.6 BTU/lb), 1755 R, and 9.152 respectively, as determined by UTC-CSD.

Figure 5 shows the fuel regression rate distribution along the fueled wall. The measured data are for chamber spinrates between 0 and 35,000 rpm. In this case, the solid fuel did not contain ammonium perchloride (AP) as an oxidizer additive. The effect of axial spin of the combustion chamber was found to be insignificant. The present computations for solid fuel without AP reproduce average or mean fuel regression rates reasonably well. At the beginning of the fuel grain behind the injector, the computed regression rate is larger than measured. However, the overall trend is similar including the peak regression rate at the flow reattachment point. There are two possible explanations for this discrepancy. In the recirculating flow, radiation effects are very significant.¹² However the present code ignores this effect. Turbulence modeling for the recirculating flow in SFRJ combustors is difficult⁵ and may not be properly modeled using the present code. At the end of the combustor, only the trend of regression rate is simulated. In this region the fuel grain joins the nozzle, producing a corner flow. Possible errors in the specified wall boundary conditions as well as errors in corner flow turbulence modeling may explain the discrepancy.

Elands et. al.¹⁶ and Netzer²⁴ have measured the solid fuel regression rate in an SFRJ chamber using a connected-pipe test facility. Polyethylene (PE) fuel was used in a small-scale SFRJ configuration. The inlet diameter was 15mm (.6 inches), and the maximum chamber diameter was 45mm (1.8 inches) making the ratio of combustor to inlet diameter 3 (step height equivalent to 33% of the combustor diameter). Measurements of local

²³ Kubota N., "Survey of Rocket Propellants and Their Combustion Characteristics," *Fundamentals of Solid Propellant Characteristics*, AIAA Education Series, 1984.

²⁴ Netzer, A., and Gany, A., "Burning and Flameholding Characteristics of a Miniature Solid Fuel Ramjet Combustor," AIAA-88-3044, Proceedings of the 26th AIAA Aerospace Sciences Meeting, January 11-14, 1988, Reno, NV.

regression rate on the fuel grain were taken using a non-intrusive ultrasonic method. The effect of inlet air mass flow, inlet air temperature, and chamber pressure on fuel regression rate were studied.

For comparison to the present code the values of fuel molecular weight, density, vaporization temperature, and heat of vaporization were taken as 28.05 grams/mole (for C_2H_4), .8008 grams/cc (50.0 lb/ft³), 1440 R, and 4.0009×10^6 Joules/kg (1719.9 BTU/lb), respectively. The inlet air temperature was 540 R. Figure 6 shows that the average fuel regression rate, over the fuel grain length, increases slightly for increased inlet air mass flow rate. The results of a finite rate chemistry code, reported in Reference 16, and the present diffusion flame code are also shown. The present code does not require thermodynamic burning rates for the PE fuel. However, since PE is a simple hydrocarbon fuel, these rates are available for finite rate models. Both combustion models reproduce the trend and magnitude of the data. The computational grid used by the present code, 338 x 44, was more dense than the grid used by the finite rate code, 20 x 20. The present code required 0.7 to 1.0 hours per solution on a CRAY X-MP/48 computer.

VI. RESULTS AND DISCUSSION

The present computational fluid dynamics code and combustion model was used to simulate the reacting flowfield in the axisymmetric combustion chamber of a 75mm SFRJ projectile (Figure 1). The solid fuel used in this chamber is the same as that described in Section V.2. In this section detailed computed results are presented for the flame location, flow velocity and mass fraction profiles, and thrust.

1. Inlet and Fueled-Wall Boundary Conditions

Several experimental and computational studies^{3,4,5} of SFRJ internal flows, without combustion, have revealed subsonic flow in the combustion chamber for small nozzle throat diameters. Consider an inert SFRJ with a 1.1 inch nozzle throat diameter and a freestream Mach number of 4.03. The nozzle is choked, and a normal shock is attached to the leading edge of the inlet.^{4,5} These conditions are also characteristic of a fueled SFRJ with combustion but with a larger nozzle throat diameter (1.6 inches) and the same Mach number.¹⁷ However, the cold flow measurements and computations for an inert SFRJ with a 1.6 inch nozzle throat diameter show supersonic internal flow (unchoked).^{4,5} In a fueled SFRJ with combustion, it can be assumed that the 1.6 inch diameter nozzle yields choked internal flow (i.e. leading-edge normal shock) just as the 1.1 inch diameter nozzle in an inert SFRJ. Hence, computational results for the 1.1 inch nozzle (subsonic internal flow and choked nozzle)⁵ with non-reacting flow can be used to provide inlet plane flow profiles for the present combustion model.

Computations are presented for the 75mm SFRJ with 1.7 inch injector and 1.6 inch nozzle throat diameters. Non-reacting flow computed results (wind tunnel test conditions with Mach number 4.03 and Reynolds Number 20 million per foot) for a 1.1 inch nozzle diameter show that the flow velocity, pressure, density and temperature are nearly constant

across the entrance to the combustion chamber (except very close to the wall). Average values for these flow variables are 84.40 m/sec (276.92 ft/sec), 18192.8 kg/m² (3725.76 lb/ft²), 2.201 kg/m³ (.00427 slug/ft³), and 510.2 R, respectively. These values are taken as sufficient upstream conditions for the present simulation. The upstream flow is assumed to consist entirely of air and is unaffected by flow conditions downstream. The Reynolds number is 3 million per foot, based on the entrance flow. A The Prandtl and Schmidt numbers are assumed to be unity. A Prandtl number (Pr) of unity is considered adequate for gaseous flows, even with combustion¹¹. A Schmidt number (Sc) of unity implies that the viscous transport of momentum acts in the same manner as the diffusive transport of mass. Thus the Lewis number, $Le = Sc/Pr$, is also unity which implies that the energy transfer due to conduction is equal to that due to diffusion. These assumptions are typical of combustion models such as the Shvab-Zeldovich formulation.¹³

The mixture fraction boundary conditions on the fueled wall are $f_{fo} = 1$, $f_{fp} = 1$, and $f_{op} = -n$. Thus, oxidizer and products are not present at the fueled wall. The wall temperature is equivalent to the fuel vaporization temperature, which is constant. A temperature dependent fuel mass fraction boundary condition on the wall could be implemented in the code. However, experimental evidence has shown that this condition does not represent the nature of combustion at the fueled wall¹⁷. The combustion of fuel over the entire wall is started and sustained by the recirculating flow behind the injector step. The entire length of fuel grain is either burning or extinguished (although the burning rate may be a function of position along the wall). Thus, after combustion is started, the fuel grain is insulated from the temperature of the airstream. Since the present combustion and flow model assume a steady state, fuel ignition and burnout (due to depletion of the fuel supply) are not considered.

2. Computational Grid

The computational grid used to discretize the flowfield consists of 185 points between the inlet plane (at the leading edge of the injector, $x = 0$) and the nozzle throat ($x = 5.942$ inches). Between the centerline and the wall of the combustion chamber (1.1 inches maximum radius), 35 points are distributed. The grid point distribution is essentially uniform in both directions. Radial wall spacings of .02 inches at the injector, .03 inches at the center of the combustion chamber (maximum radius), and .02 inches at the nozzle throat are used. In the streamwise direction an average grid spacing of .03 inches is used. The grid distribution should be adequate since the turbulence model is not based on wall functions, which require exceptionally fine wall grid clustering. A finer grid with essentially half the wall spacing did not change the results to a noticeable degree, but the computer run times were substantially increased.

Converged solutions were obtained after about 843 iterations and approximately 15 minutes of CPU time on a CRAY X-MP/48 computer. Convergence was determined using Equation B16 with λ_1 set to .005. No under-relaxation was required, thus $a_{ur} = 1$.

3. Mean Flow Features

Figure 7 shows the velocity vectors in the vicinity of the injector. The flow directed toward the fueled wall separates behind the backward-facing step. The incoming flow is deflected toward the symmetry axis of the chamber. The separated flow is decelerated near the wall while the deflected airstream retains most of the inlet velocity. The separated flow reattaches on the fueled wall at about .25 inches from the inlet, thus the length of the recirculation zone is about .15 inches or 3% of the chamber length. This is the only region of recirculating flow in the chamber.

Figure 8 shows the velocity vectors in the vicinity of the nozzle entrance. The flow near the fueled wall stagnates, but it does not separate in the corner of the forward-facing step. The flow away from the wall turns sharply toward the combustor centerline. As a result, mean flow plays a significant role in transporting fuel from the wall to the core flow. In contrast, turbulent flow convection is the dominant transport mechanism along most of the fueled wall where the flow is parallel to the wall. In the recirculation region behind the injector, recirculation works against convection in transporting fuel into the core flow.

4. Combustion Flame

Figure 9 shows the temperature contours across the combustion chamber. The highest temperature contour shown is $T = 4297$ R which is equivalent to the flame temperature assumed in the computation. The concentration of high temperatures at the beginning of the chamber indicates that the flame is attached to the edge of the injector. Thus the flame is "held" by the injector or flameholder. The temperature gradients at the flameholder are large (i.e. closely spaced contours). This result is typical of diffusion-flame combustion models where the reaction rate time lag is zero. The flame extends to the nozzle and intersects the chamber exit plane about midway between the axis and the nozzle wall. The flow between the flame and the chamber axis rapidly cools. The flow between the flame and the fueled wall cools gradually to the fuel vaporization temperature of about 1773 R. Most of the heat produced by the reaction is found between the flame and the wall. These temperature contours are functions of the fuel molecular weight and the thermodynamic data used in the computation.

5. Flow Profiles

Figure 10 shows streamwise (u) velocity profiles for four stations between the injector and the nozzle throat. The first station ($x = .136$ in.) is located at about the center of the recirculation region, behind the injector. The second ($x = 2.038$ in.) is located at about chamber midpoint. The third ($x = 5.572$ in.) is located near the nozzle entrance. The fourth ($x = 5.942$ in.) is located at the nozzle throat. The no-slip wall boundary condition and the zero-radial-gradient axis boundary condition are illustrated. Salient features of the developing flow are: separation behind the injector step ($x = .136$ in.), flow stagnation (but no separation) near the wall before the nozzle entrance ($x = 5.572$ in.), and flow acceleration along the chamber axis (from about 310 to 1000 ft/s). The radial location

of the flame is indicated by a maximum in each velocity profile, which moves toward the chamber axis as the location of the profile moves downstream.

Figures 11 thru 13 show profiles of mass fractions (m_{fo} , m_{fp} , and m_{op}) at three axial locations. At each axial station, the flame location is indicated by $m_{pr} = 1$, $m_{fu} = 0$, and $m_{ox} = 0$. Since it is assumed that the reaction goes to completion, the mass fraction of fuel is zero between the flame and the symmetry axis, and the mass fraction of oxidizer is zero between the flame and the fueled wall. The flame location changes from about $y = .85$ to $y = .50$ inches from the axis between the injector and the nozzle throat.

Figures 14 and 15 show the temperature and density profiles. At each axial location, the radial location of the flame is indicated by the temperature peak. This peak is about 4300 R and is nearly constant from the injector to the nozzle throat. The density profiles also serve as a means to track the radial location of the flame. The flow density reaches a minimum in the flame, about 7% of the inlet air density. The flow density near the fueled wall varies considerably along the length of the chamber.

6. SFRJ Flight Performance

Mermagen and Yalamanchili^{1,2} have conducted free-flight tests of 75mm SFRJ projectiles. A Hawk radar/doppler velocimeter was used to measure the velocity histories of rounds with different injector, nozzle throat diameters, and solid fuels (including inert rounds). All fueled rounds demonstrated successful autoignition with burn times varying between 1.6 and 2.5 seconds. Suitable repeatability of fuel burn time and velocity performance was reported.

The velocity history and drag versus Mach number data for a typical fin-stabilized (FS) SFRJ projectile are shown in Figures 16 and 17. The solid fuel in these projectiles contained AP. The effect of ramjet burn are shown as nearly a constant C_D between Mach number 3.6 and 4.0 in Figure 17 and gradual retardation in velocity between 0 and 1.6 seconds (burn time) in Figure 16. The FS-SFRJ has a longer combustion chamber (fuel grain) than the spin-stabilized version. In addition, the FS-SFRJ has nearly zero axial spin in flight.

The ramjet thrust is defined from this data as,

$$\text{Thrust} = \frac{1}{2} \rho V^2 S_{\text{ref}} \Delta C_D \quad (13)$$

where ρ is the air density, V is the velocity along the trajectory, S_{ref} is the reference area with a reference diameter of 75mm, and ΔC_D is the difference in drag coefficient between live and inert SFRJ projectiles at the same Mach number. Figure 18 shows the thrust as determined from Equation 13. The SFRJ projectile generates about 250 pounds of thrust during the 1.6 second burn time.

The present steady-state combustion model can predict the SFRJ burn time from the solid fuel regression rate and the thickness of the solid fuel layer,

$$\text{burn time(sec)} = \frac{t_{\text{fu}}(\text{in})}{\dot{r}(\text{in/sec})} \quad (14)$$

where t_{fu} and \dot{r} can be average values over the fuel grain. The drag coefficient is computed from the change in momentum from the injector (combustion chamber inlet) to the nozzle,

$$\frac{\Delta \text{Momentum}}{1/2\rho V^2 S_{\text{ref}}} = C_D = \frac{\int \int_{S_1} \rho_1 \vec{V}_1 (\vec{V}_1 \cdot \hat{n}_1) dS - \int \int_{S_2} \rho_2 \vec{V}_2 (\vec{V}_2 \cdot \hat{n}_2) dS}{1/2\rho V^2 S_{\text{ref}}} \quad (15)$$

where subscripts 1 and 2 refer to the injector and nozzle, respectively. For the inert (unfueled) projectile, for which the internal flow is supersonic and an oblique shock wave is attached to the leading edge of the inlet, C_D was obtained from Reference 5. For the live projectile, the internal flow is subsonic with combustion and with an attached normal shock at the leading edge of the inlet. C_D was obtained from Reference 5 for the exterior and inlet and from the present code for the combustion chamber.

The computed results are shown with measurements in Figure 18. The computed burn time is 1.9 seconds, 18% longer than the 1.6 seconds observed. The computed thrust is 210 pounds, 16% smaller than the average measured thrust of 250 pounds. Although the projectile decelerates during the burn time, the computation assumes a steady-state burn and thus the launch velocity of 4500 ft/sec is used. Since fuel oxidizer (AP) effects are not included in the combustion model the computation overestimates the burn time and underestimates the thrust. Connected-pipe tests¹⁷ show that the addition of AP (with catalyst) to solid fuel increases the regression rate by about 40% and thus decreases the burn time by about 40% in a non-spinning SFRJ. Thrust measurements are not available, however AP should increase the thrust generated by an SFRJ due to an increased fuel flow rate. Flight tests of solid fuels without AP in SFRJ projectiles have not been reported. Sources of discrepancy between measured and computed flight performance include: the effects of radiation which are excluded from the combustion model, uncertainty in the thermodynamic input quantities, and the validity of the diffusion flame model. Efforts should be made to incorporate the effects of AP for non-spinning flight cases.

VII. CONCLUSIONS

A steady flow solution of the Navier-Stokes equations is linked with a diffusion-flame combustion model for a one-step, irreversible, mass-controlled reaction between solid fuel and air. The reaction is assumed to go to completion and to produce products that are treated as a single specie. A one-equation, algebraic turbulence model for combustor flows is employed. Solutions produced by this code are applied to the subsonic flow, solid fuel combustion within a SFRJ projectile. The results provide estimates of the major features of the internal flow including flow recirculation, flame position, exit plane flow, burn time, and thrust. The quality of the results are dependent on the accuracy of the thermodynamic input data. Since the code assumes a mass-controlled reaction, reaction rate data is not required. Thus the code can be applicable to the wide range of solid fuels commonly used in SFRJ. Computer requirements on a Cray X-MP/48 range from .25 to 1.0 CPU hours per solution, making the code suitable for SFRJ combustor design studies. This application

of a diffusion-flame combustion code serves as a logical first step to detailed combustion modeling of reacting flow in SFRJ projectiles. The addition of radiation and fuel oxidizer (AP) effects could improve the utility of the simulation.

Major observations on the combustion in a SFRJ from computed results include:

1. The injector serves as a flameholder, in that the flame is attached to the injector and extends downstream into the combustion chamber.
2. At any axial position along the chamber the location of the combustion flame is indicated by a temperature maximum, a density minimum, and the mass fraction of fuel, oxidizer and products equal to 0, 0, and 1 respectively.
3. If the flame does not reach the chamber axis at the nozzle throat, the flow at chamber exit will consist of accelerated air, flame, diluted and unburned fuel, and combustion products. Thus the exit flow may not be entirely energized by combustion.

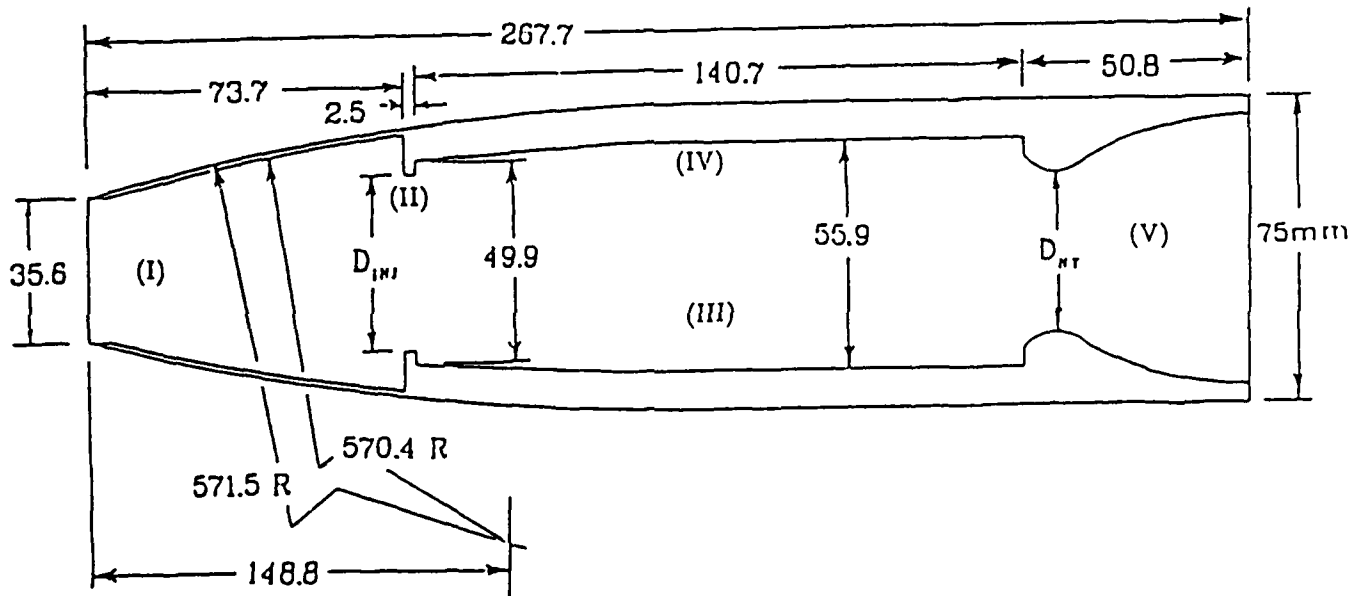
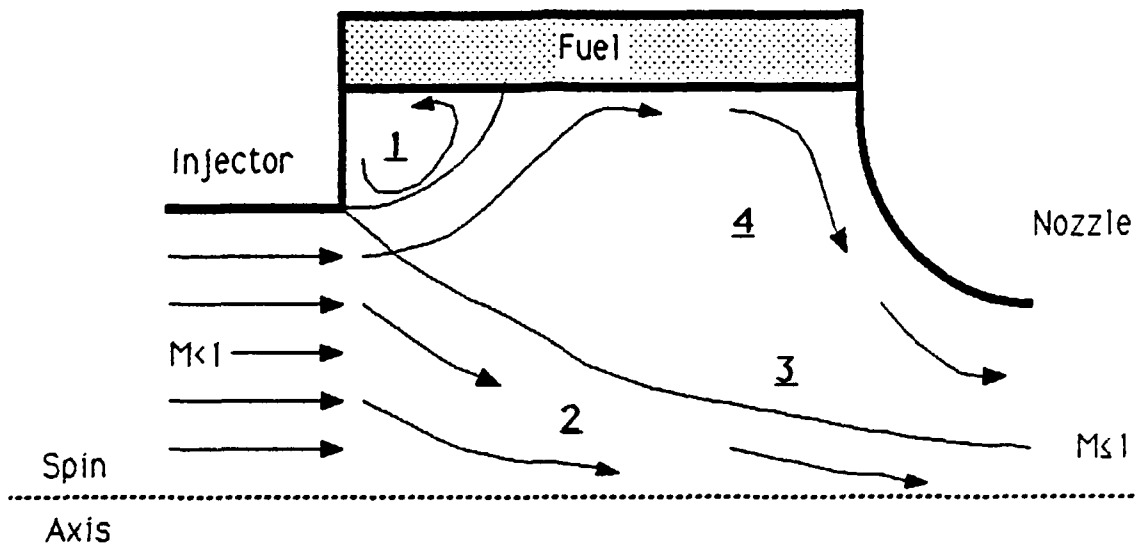


Figure 1. SFRJ Geometry; Dimensions in Millimeters, $D_{inj} = 43.2$ mm, $D_{nt} = 40.6$ mm. (I) Inlet, (II) Injector, (III) Combustion Chamber, (IV) Fueled Wall, (V) Nozzle.



- (1) RECIRCULATING (SEPERATED) FLOW
- (2) PRODUCTS AND UNCONSUMED OXIDIZER
- (3) FLAME, PRODUCTS ONLY
- (4) PRODUCTS AND UNCONSUMED FUEL

Figure 2. Schematic of Steady-State Combustion in the Chamber of an SFRJ.

Variation of Laminar Reattachment Length
with Reynolds Number (Inert Flow)

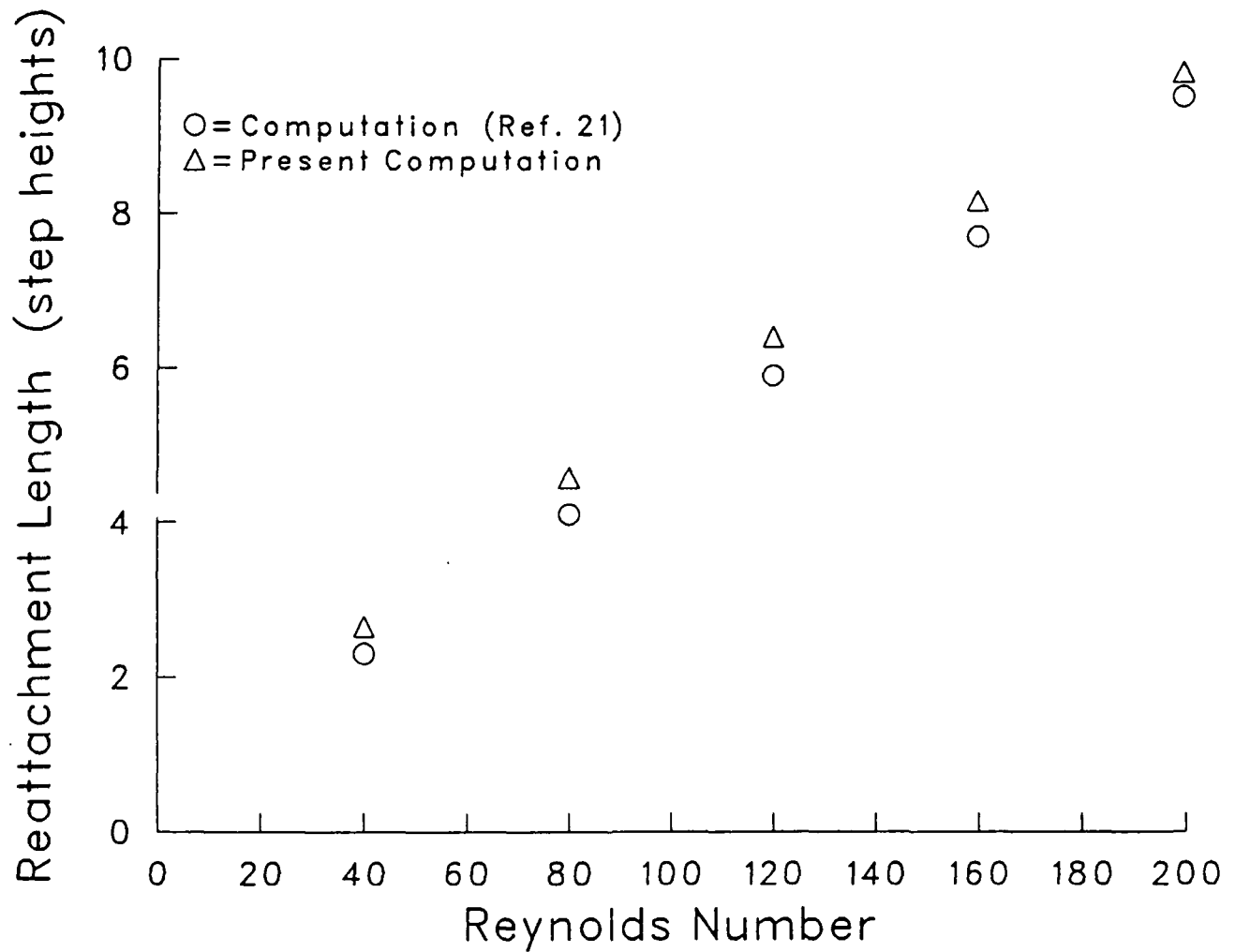


Figure 3. Variation of Laminar Reattachment Length with Reynolds Number, Inert Flow, $Re = 40$ to 200

Variation of Reattachment Length with Spinrate
in a Sudden-Expansion Combustor (Inert Flow, $Re = 31000$)

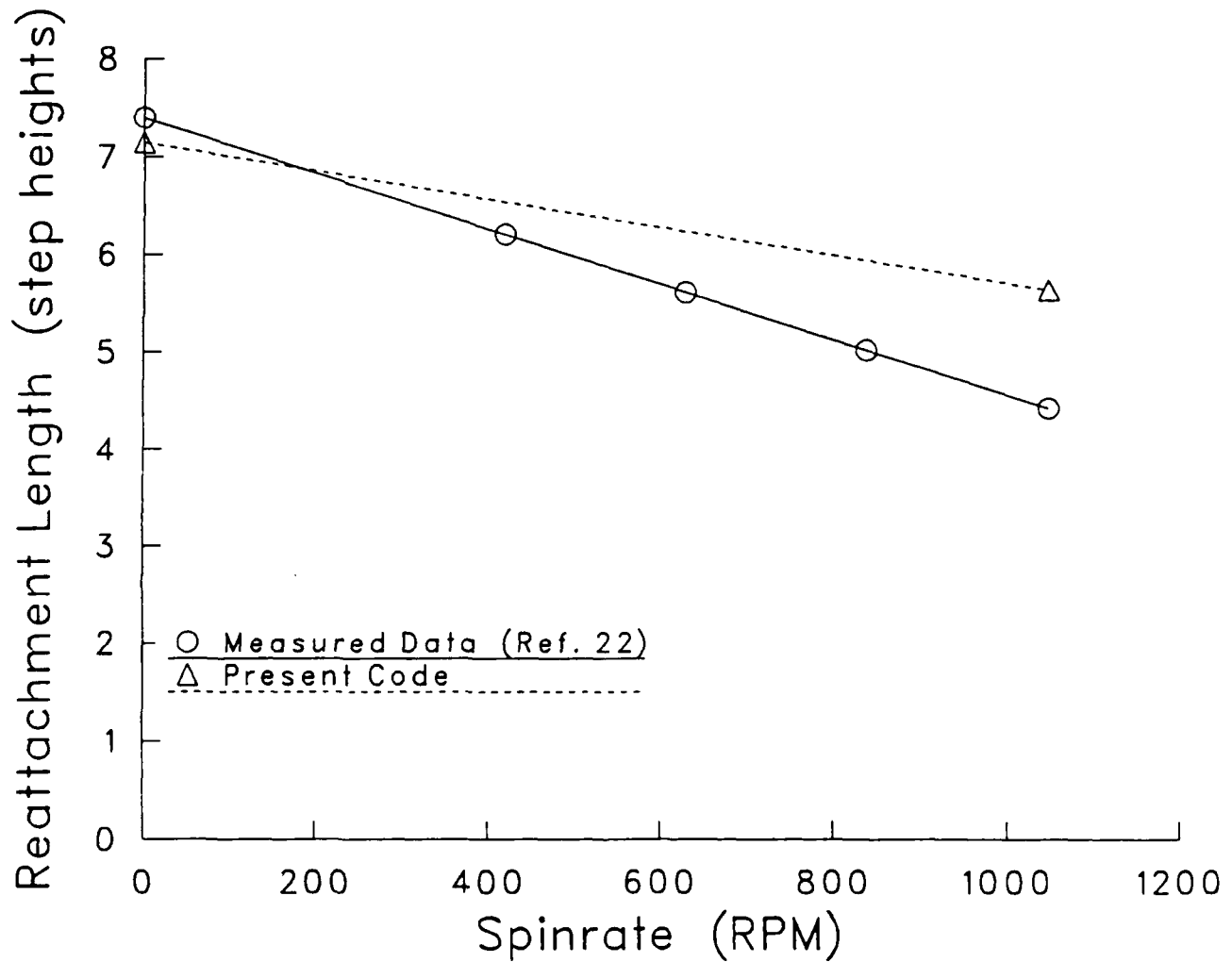


Figure 4. Variation of Reattachment Length with Spinrate, Inert Flow, $Re = 31000$.

Regression Rate Distribution Along the Fueled Wall
for a SFRJ Connected-Pipe Test

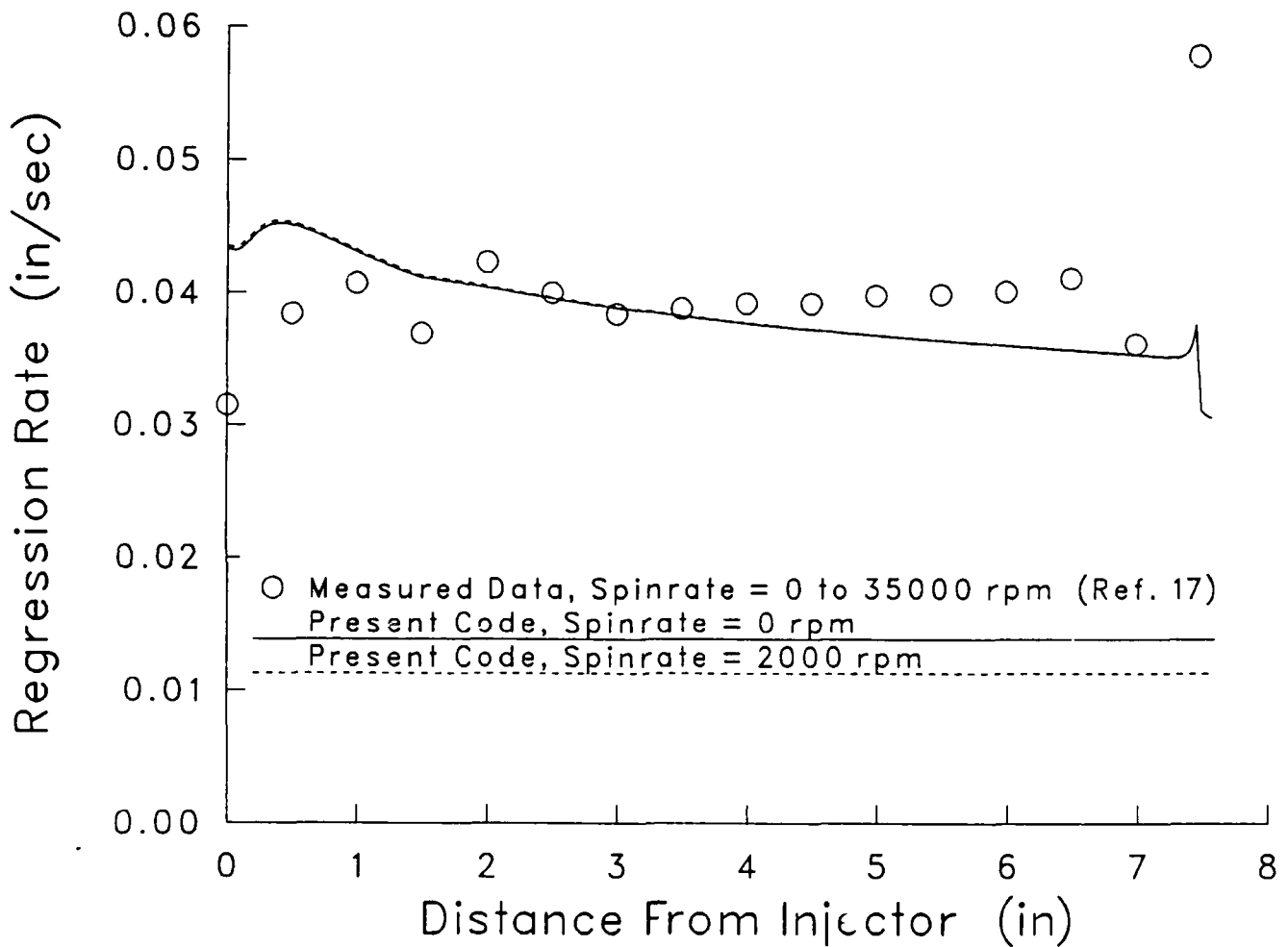


Figure 5. Regression Rate Distribution Along the Fueled Wall of a SFRJ; Connected-Pipe Test.

Variation of Fuel Regression with Mass Flow Rate
SFRJ Combustor, Polyethylene Fuel

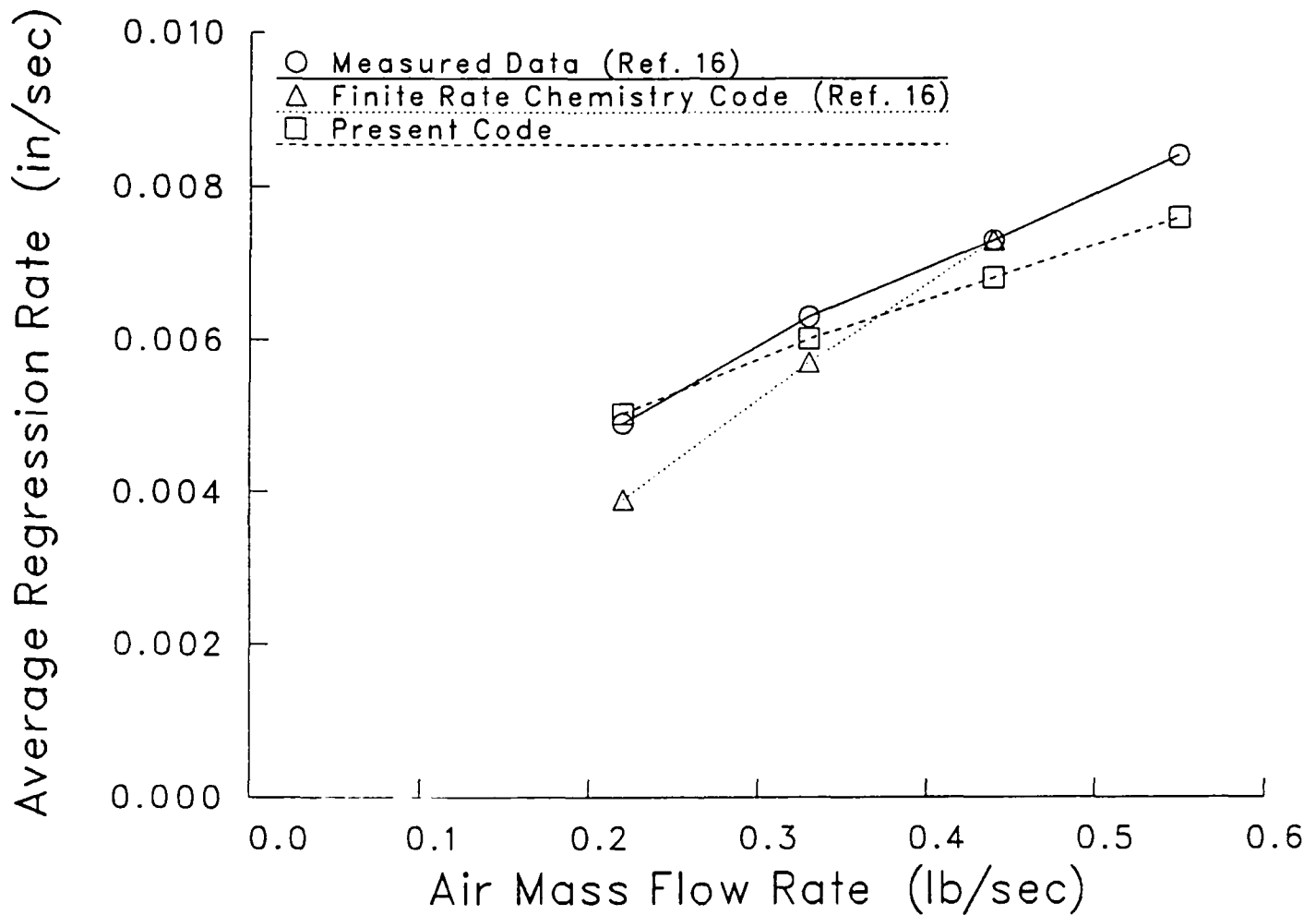


Figure 6. Variation of Regression Rate with Mass Flow Rate in a SFRJ; Connected-Pipe Test.

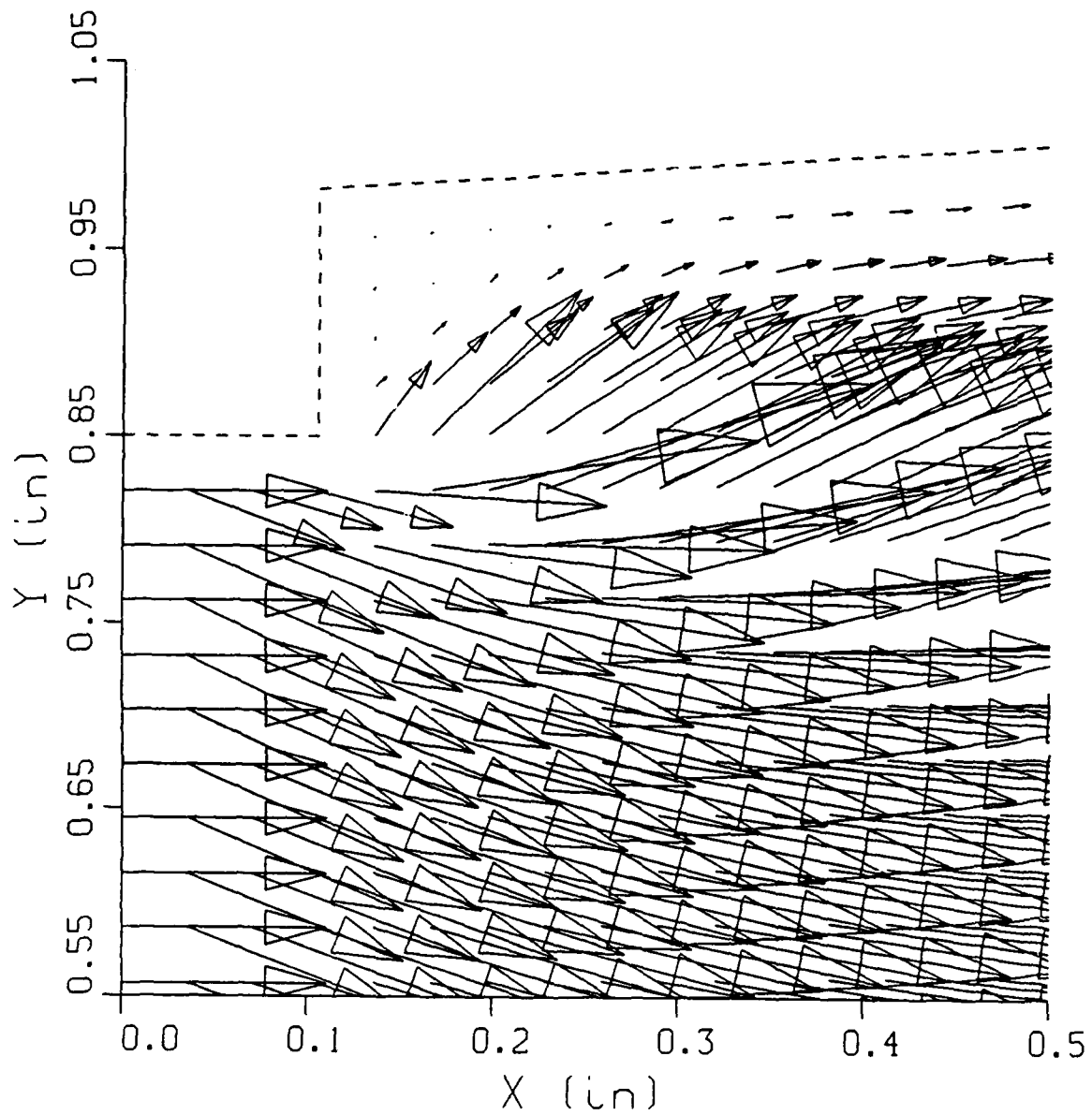


Figure 7. Computed Velocity Vectors for the Flowfield Near the Injector of a SFRJ.

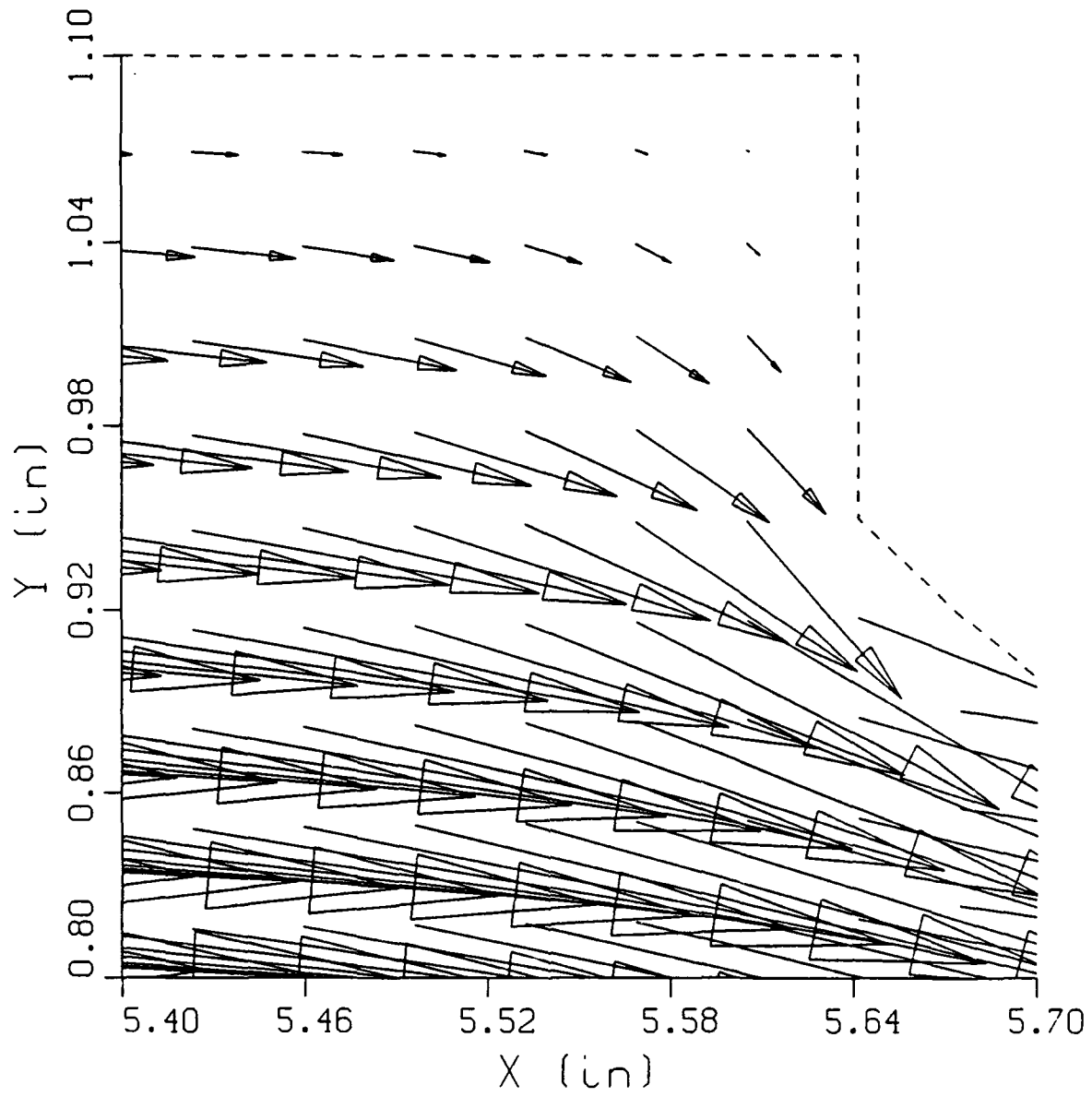


Figure 8. Computed Velocity Vectors for the Flowfield Near the Nozzle of a SFRJ.

Temperature (R)

Δ = 716

\square = 1432

∇ = 2148

\diamond = 2864

$+$ = 3580

\times = 4297

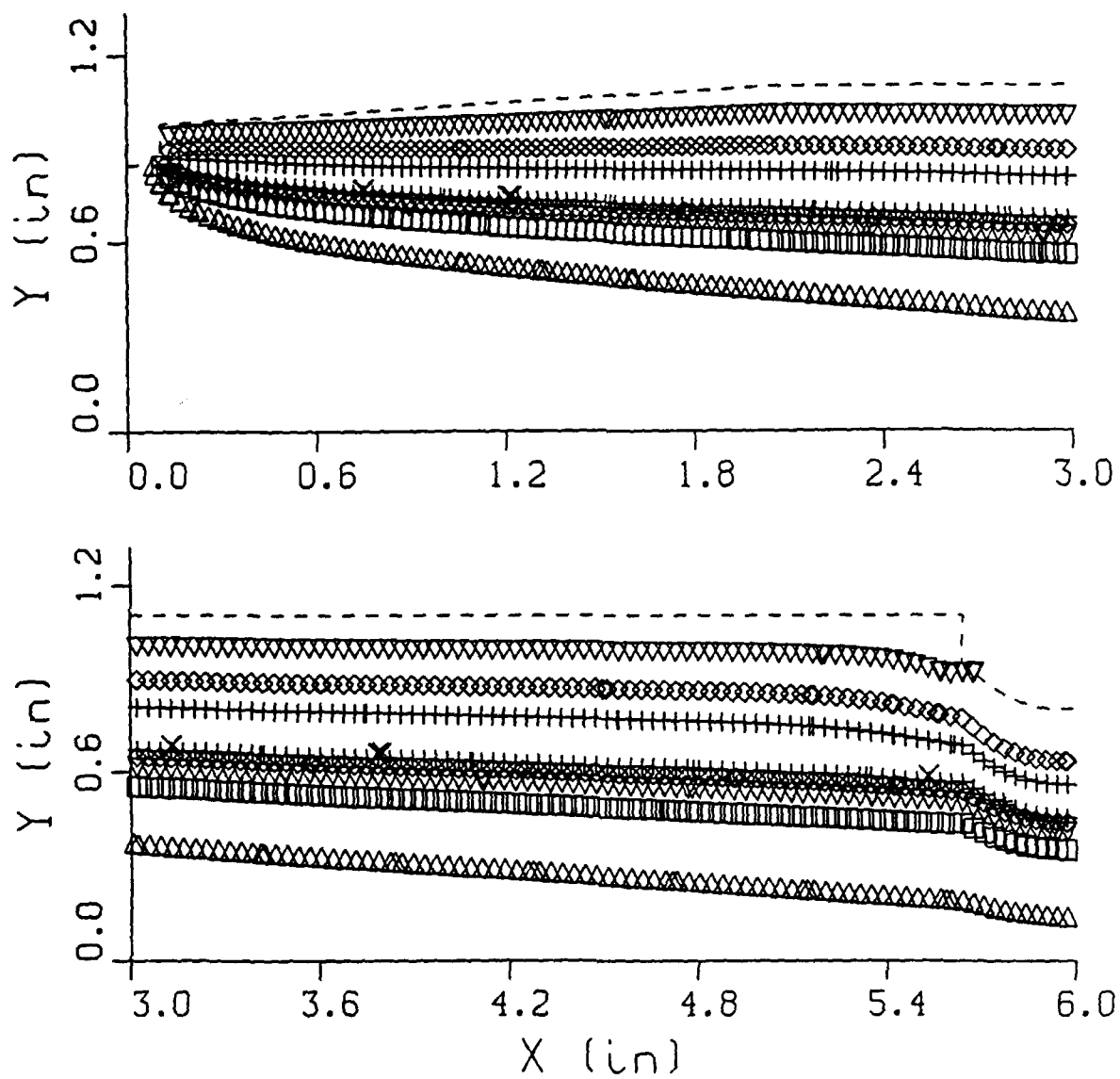


Figure 9. Computed Temperature Contours.

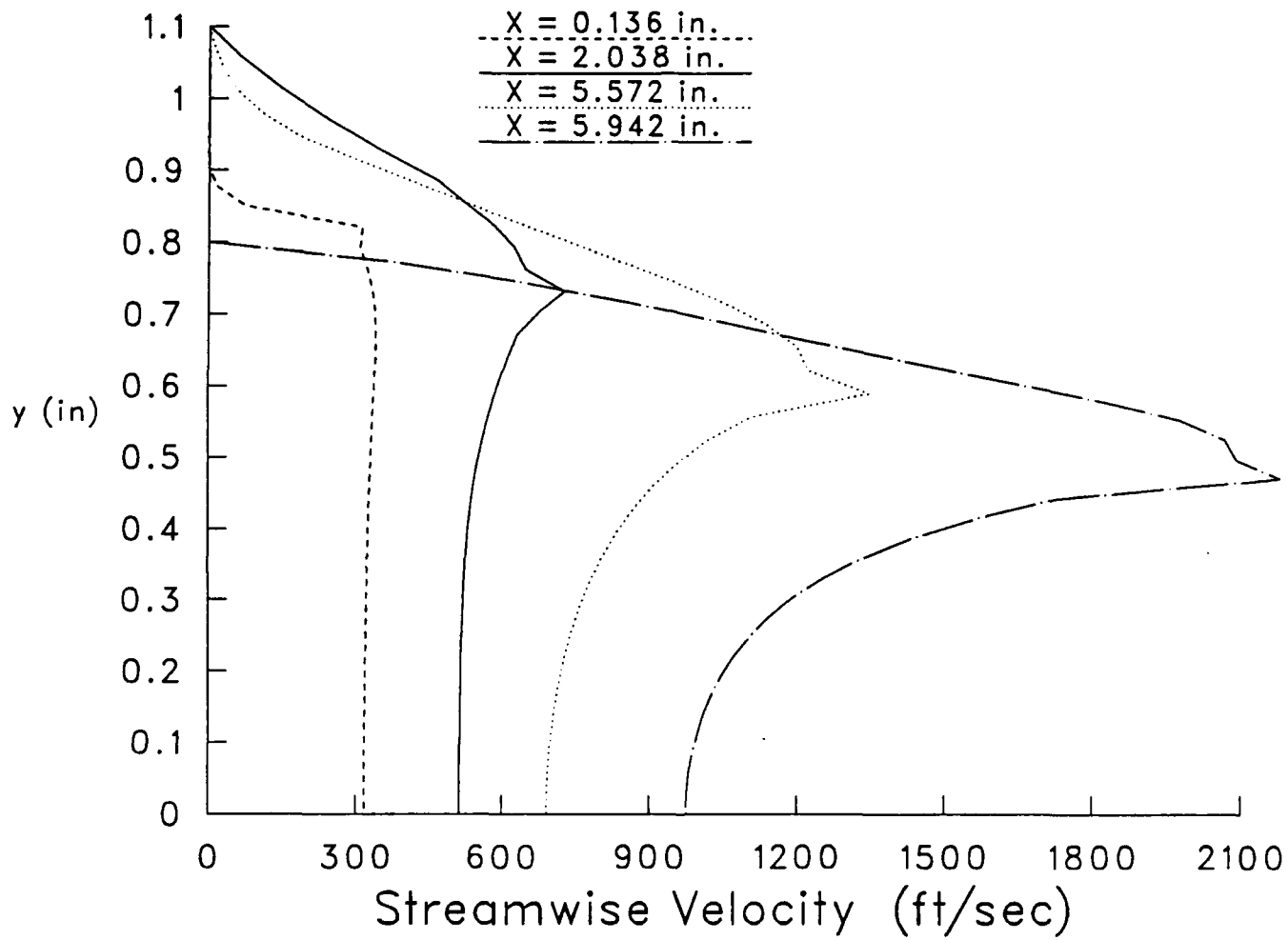


Figure 10. Computed Streamwise Velocity Profiles.

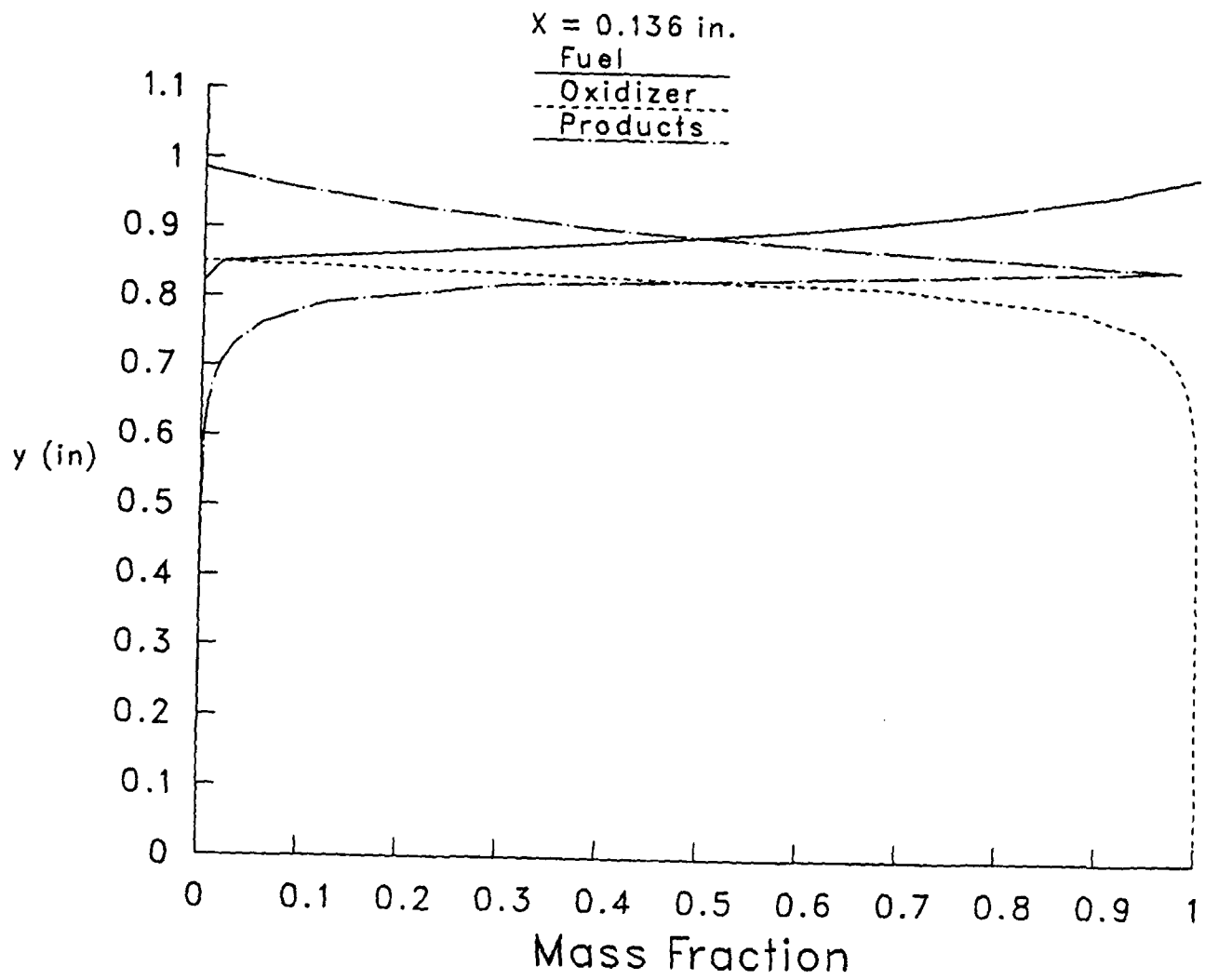


Figure 11. Computed Mass Fraction Profiles; $X = 0.136$ inches.

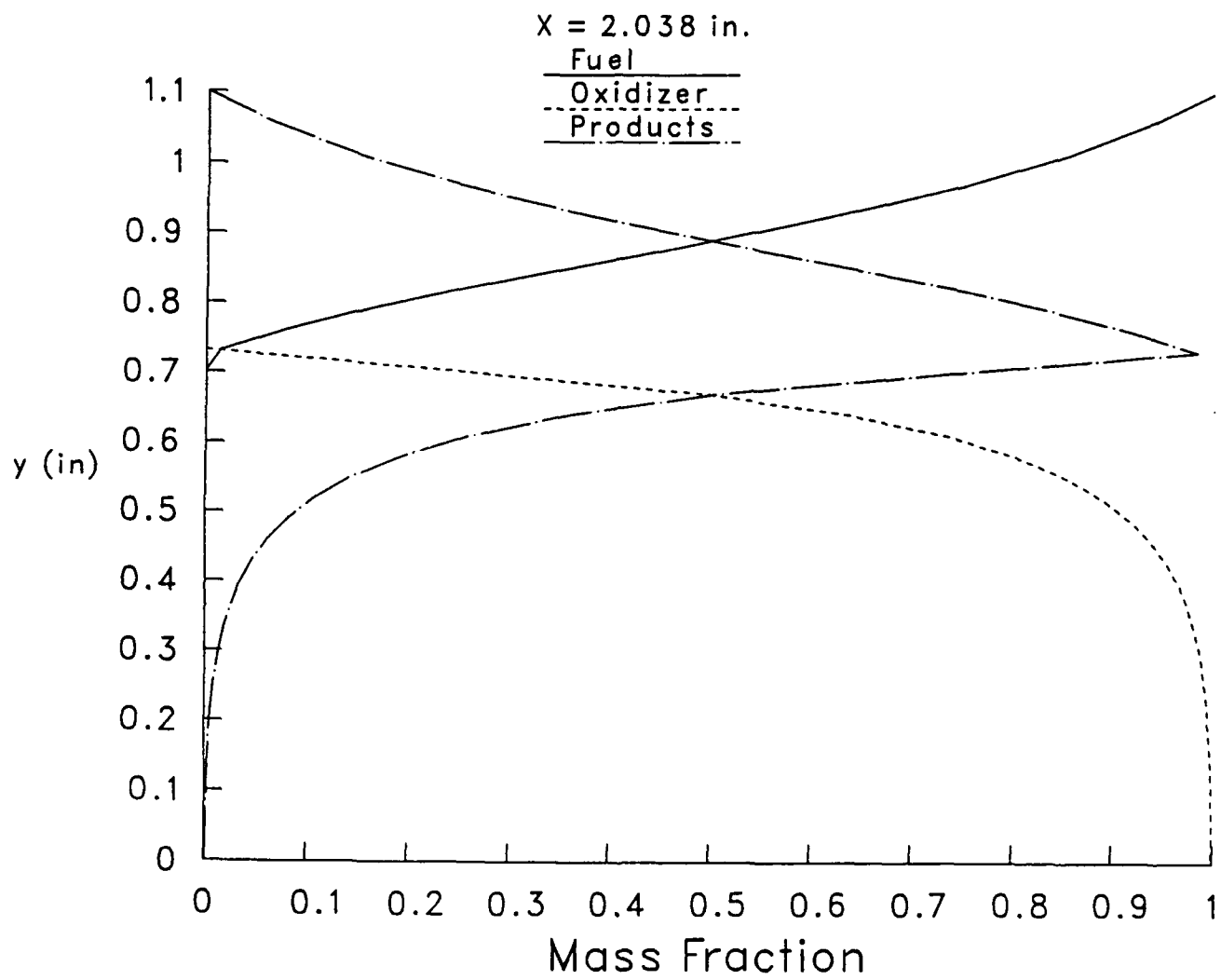


Figure 12. Computed Mass Fraction Profiles; X = 2.038 inches.

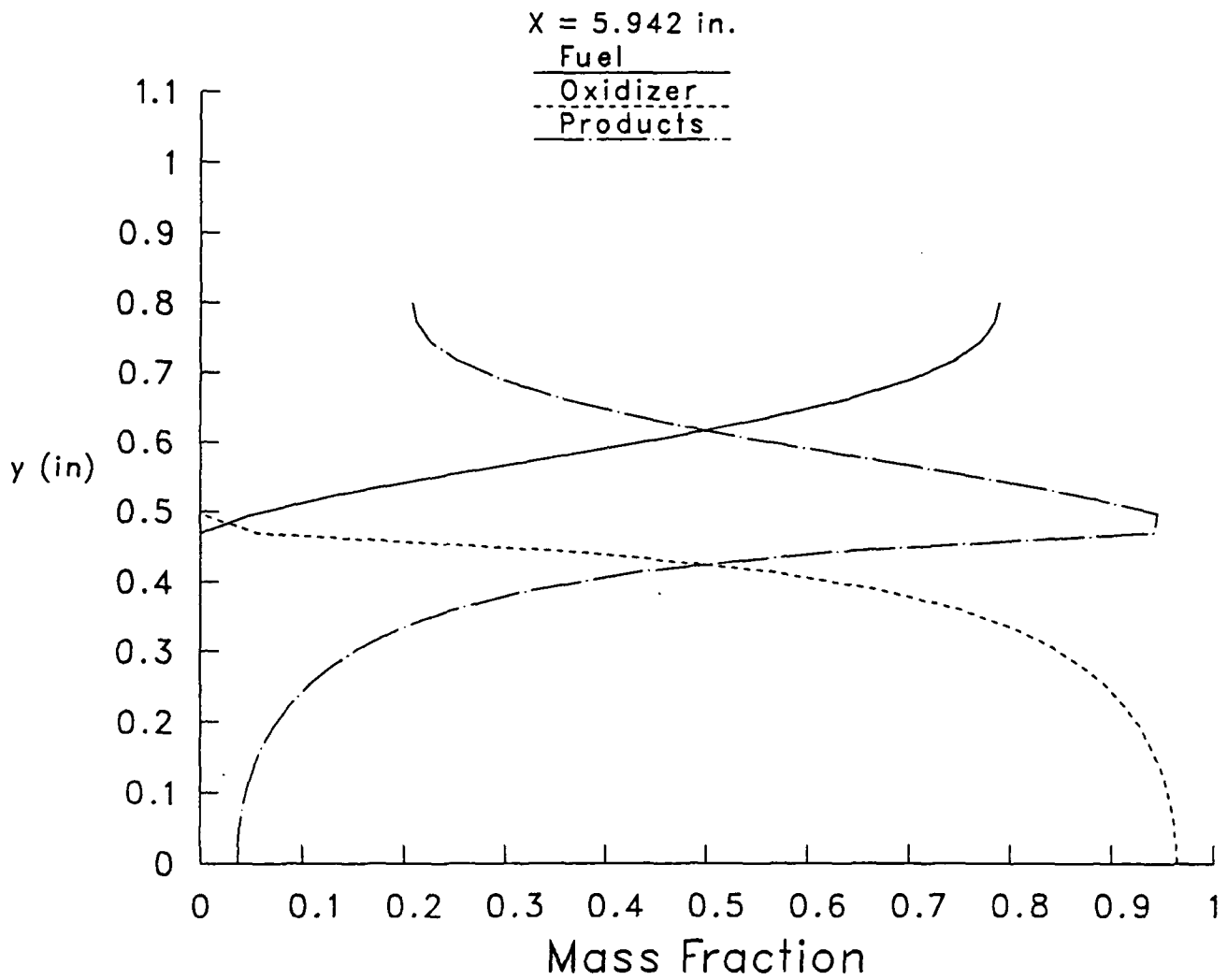


Figure 13. Computed Mass Fraction Profiles; X = 5.942 inches.

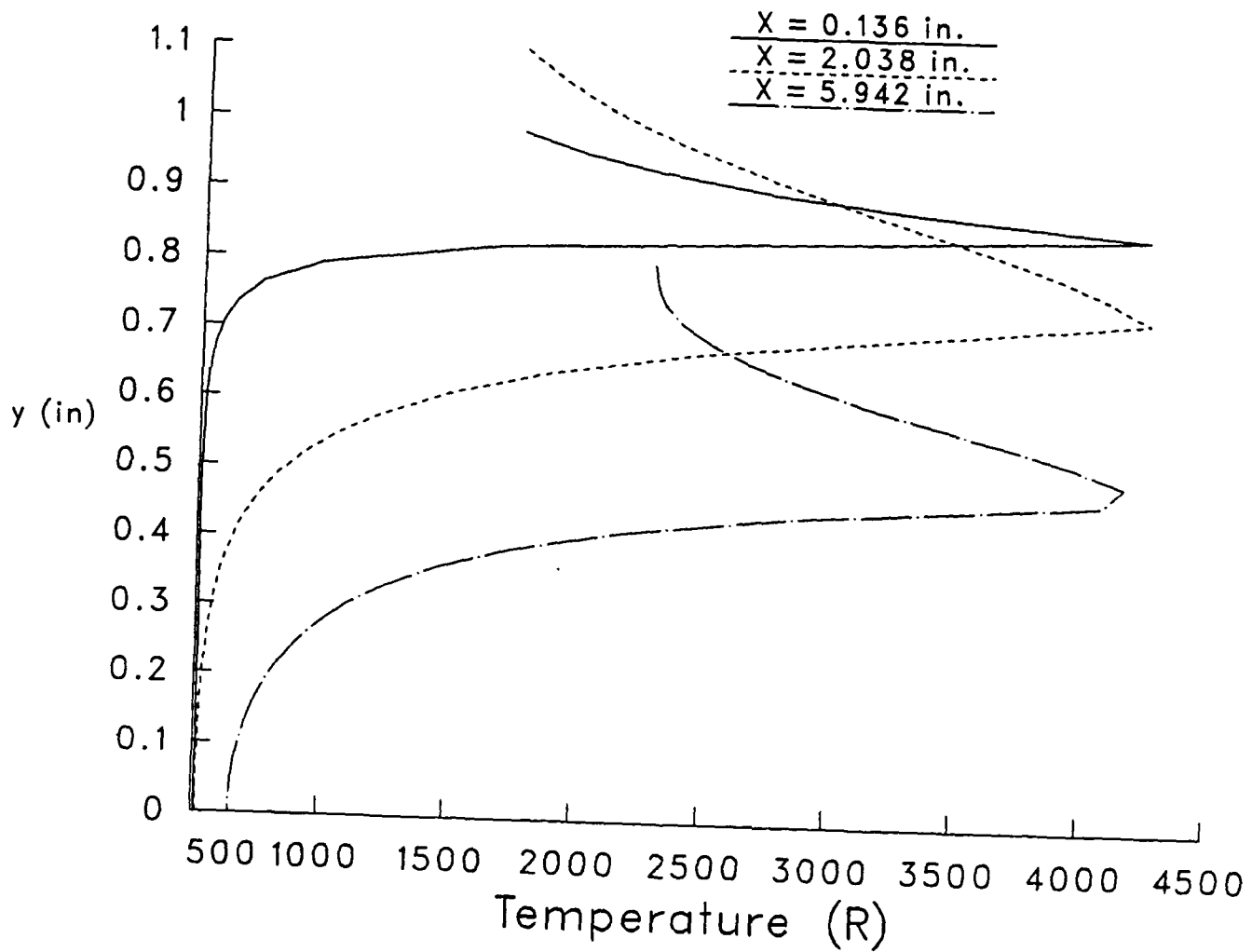


Figure 14. Computed Temperature Profiles.

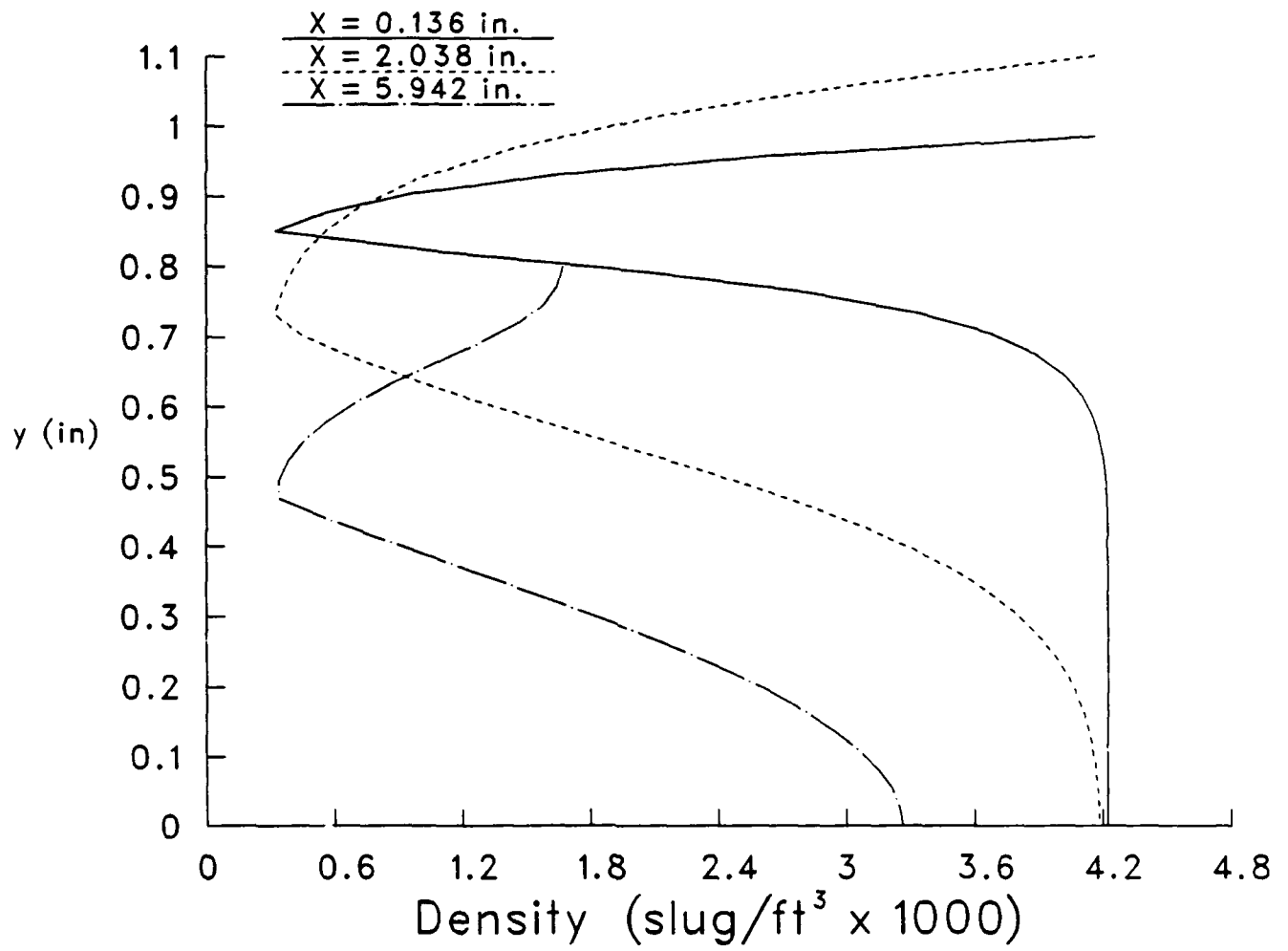


Figure 15. Computed Density Profiles.

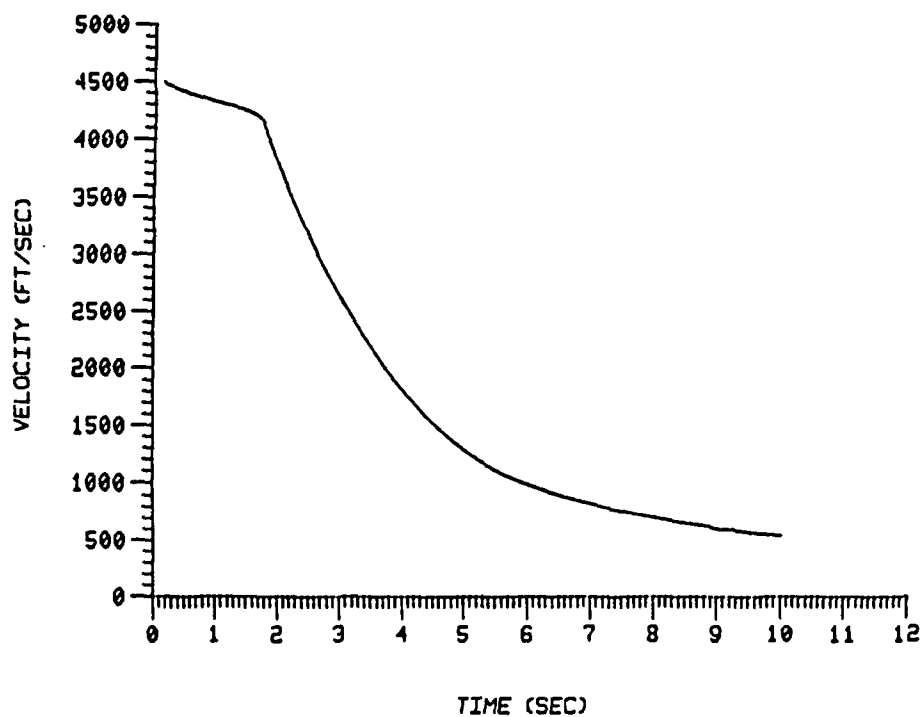


Figure 16. Velocity-Time History of Fin-Stabilized SFRJ Round 26362.

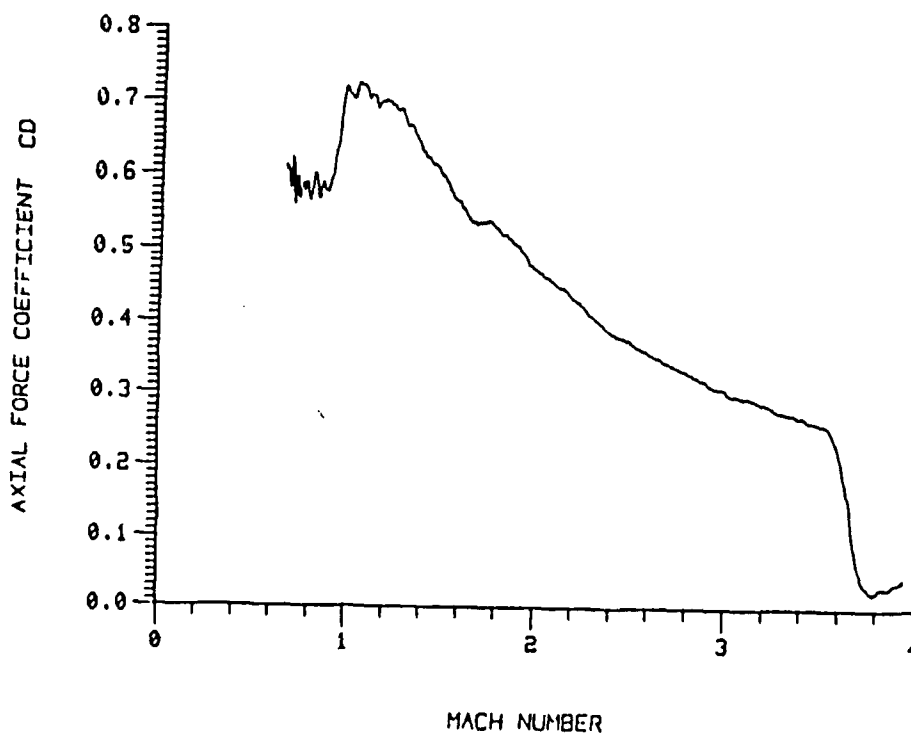


Figure 17. Drag Coefficient vs. Mach Number for Fin-Stabilized SFRJ Round 26362.

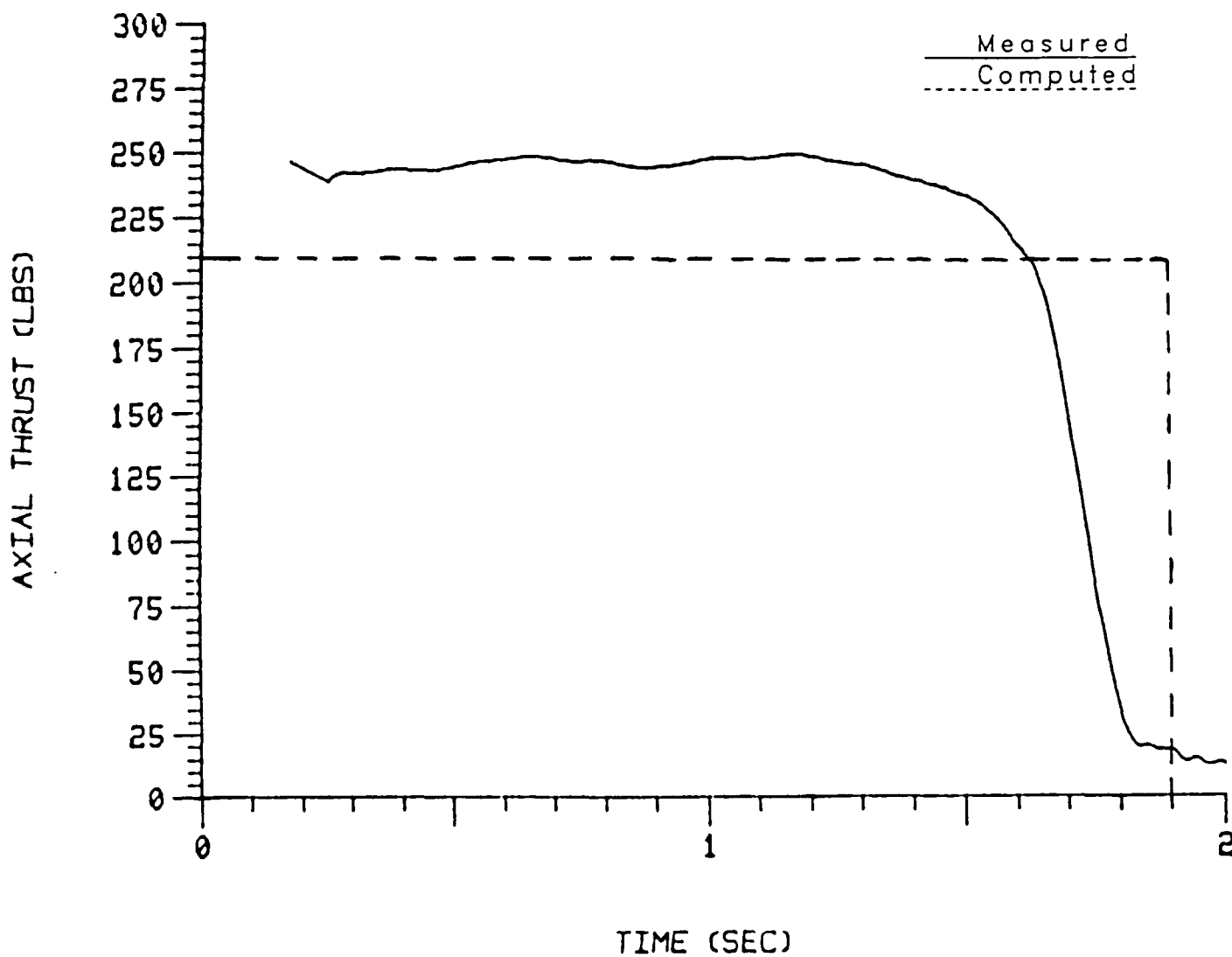


Figure 18. Thrust vs. Time for Fin-Stabilized SFRJ Round 26362; Measured and Computed.

References

1. Mermagen W.H., and Yalamanchili R.J., "First Diagnostic Tests of a 75mm Solid Fuel Ramjet Tubular Projectile," ARBRL-MR-03283, U.S. Army Ballistic Research Laboratory, Aberdeen Proving Ground, MD, June 1983. (AD A130598)
2. Mermagen W.H., and Yalamanchili R.J., "Experimental Tests of a 105/75mm Solid Fuel Ramjet Tubular Projectile," ARBRL-MR-3416, U.S. Army Ballistic Research Laboratory, Aberdeen Proving Ground, MD, December 1984. (AD B089766)
3. Nusca, M.J., and Oskay, V.O., "Comparison of Computational Analysis with Flight Tests of a 40mm Solid-Fuel Ramjet Projectile," U.S. Army Ballistic Research Laboratory, Aberdeen Proving Ground, MD, Technical Report in publication.
4. Kayser L.D., Yalamanchili R.J., and Trexler C., "Pressure Measurements on the Interior Surface of a 75mm Tubular Projectile at Mach 4," ARBRL-MR-3725, U.S. Army Ballistic Research Laboratory, Aberdeen Proving Ground, MD, December 1988.
5. Nusca, M.J., Chakravarthy, S.R., and Goldberg, U.C., "Computational Capability for the Solid Fuel Ramjet Projectile," ARBRL-TR-2958, U.S. Army Ballistic Research Laboratory, Aberdeen Proving Ground, MD, December, 1988.
6. Vos, J.B., "Calculating Turbulent Reacting Flows Using Finite Chemical Kinetics," AIAA Journal, Vol. 25, No. 10, October 1987, pp.1365-1372.
7. Vos, J.B., "The Calculation of Turbulent Reacting Flows with a Combustion Model Based on Finite Chemical Kinetics," PhD. Dissertation, Dept. of Aerospace Engineering, Delft University, the Netherlands, 1987.
8. Giolda, T.P., "Numerical Simulation of Chemically Reacting Solid Fuel Ramjet Internal Flowfields," Final Report for U.S. Army Ballistic Research Laboratory Contract No. DAAL03-86-D-0001, February 1988.
9. Hill, P. and Peterson, C., Mechanics and Thermodynamics of Propulsion, Addison-Wesley, 1965.
10. Khalil, E.E., Spalding, D.B., and Whitelaw, J.H., "The Calculation of Local Flow Properties in Two-Dimensional Furnaces," International Journal of Heat and Mass Transfer, 1975, Vol. 18, pp. 775-791.
11. Bradshaw, P., Cebeci, T., and Whitelaw, J.H., Engineering Calculation Methods for Turbulent Flows, Academic Press, New York, 1981.
12. Kuo, K.K., Principles of Combustion, John Wiley and Sons, Inc., New York, 1986.
13. Williams, F.A., Combustion Theory, Addison-Wesley Publishing Company, Inc., 1965.
14. Vanka, S.P., "Calculation of Axisymmetric, Turbulent, Confined Diffusion Flames," AIAA Journal, Vol. 24, No. 3, March 1986, pp. 462-469.
15. Kim, Y.M., and Chung, T.J., "Finite Element Analysis of Turbulent Diffusion Flames," AIAA-88-0062, Proceedings of the 26th AIAA Aerospace Sciences Meeting, January 11-14, 1988, Reno, NV.

16. Elands, P.J.M., Korting, P.A.O.G., Dijkstra, F., and Wijchers, T., "Combustion of Polyethylene in a Solid Fuel Ramjet - A Comparison of Computational and Experimental Results," AIAA-88-3043, Proceedings of the 26th AIAA Aerospace Sciences Meeting, January 11-14, 1988, Reno, NV.
17. MacLaren, R.O., and Holzman, A.L., "SFRJ Projectile Development," Final Report, CSD-2710-FR, United Technologies Chemical Systems Division, Sunnyvale, CA., 26 June 1981. (See also, Hussain, S.M., and Holzman, A.L., "Effects of Spin on SFRJ Projectile Performance," Monthly Progress Report No. 12, Contract No. DAAA15-86-C-0008, 1 Dec - 31 Dec., 1986.)
18. Ballal, D.R., "Combustion-Generated Turbulence in Practical Combustors," AIAA Journal of Propulsion, Vol. 4, No. 5, Sept-Oct 1988, pp. 385-390.
19. Pun, W.M., and Spalding, D.B., "A Procedure for Predicting the Velocity and Temperature Distributions in a Confined, Steady, Turbulent, Gaseous, Diffusion Flame," Imperial College, Mechanical Engineering Department Report SF/TN/11, 1967.
20. Patankar, S.V., and Spalding, D.B., "A Computer Model for Three-Dimensional Flow in Furnaces," Proceedings of the 14th International Symposium on Combustion, Pennsylvania State University, August 20-25, 1972, pp.605-614.
21. Lee, J.J., "Heat and Mass Transfer Calculations for Recirculating Laminar and Turbulent Flows in an Abrupt Pipe Expansion," AIAA-88-3791, Proceedings of the 1st AIAA/ASME/SIAM/APS National Fluid Dynamics Congress, July 25-28, 1988, Cincinnati, OH.
22. So, R.M.C., and Ahmed, S.A., "Rotation Effects on Axisymmetric Sudden-Expansion Flows," AIAA Journal of Propulsion and Power, Vol. 4, No. 3, May-June 1988, pp. 270-276.
23. Kubota N., "Survey of Rocket Propellants and Their Combustion Characteristics," Fundamentals of Solid Propellant Characteristics, AIAA Education Series, 1984.
24. Netzer, A., and Gany, A., "Burning and Flameholding Characteristics of a Miniature Solid Fuel Ramjet Combustor," AIAA-88-3044, Proceedings of the 26th AIAA Aerospace Sciences Meeting, January 11-14, 1988, Reno, NV.
25. Schlichting, H., Boundary Layer Theory, 7th ed., translated by J. Kestin, McGraw-Hill, New York, 1979.
26. Carnahan, B., Luther, H.A., and Wilkes, J.O., Applied Numerical Methods, John Wiley and Sons, New York, 1969.

Appendix A

In this appendix the conservation equations for mass, momentum and energy in a compressible fluid flow are described. In addition, equations for the conservation of chemical species and various fluid properties are derived. These equations, along with a suitable model of turbulence viscosity, form the basis of the present combustion model. The internal geometry of the SFRJ (Figure 1) promotes flow with substantial regions of low speed flow (Mach number < 1) with recirculation and swirl (for non-zero axial spin). Thus the conservation equations are elliptic in form. Due to the axisymmetric nature of the SFRJ geometry, the equations are written in cylindrical coordinates. The velocity components in this system are u, v , and w for the radial (r), azimuthal (θ), and axial (z) directions, respectively. Axisymmetric flow is assumed, thus all θ -derivatives are ignored. However, the azimuthal velocity component (v) and the azimuthal momentum equation are retained so that swirling flows can be treated. Only steady-state flows are considered, thus time derivatives ($\partial/\partial t$) are ignored as well.

For flows that are subsonic and dominated by recirculation and rotation, the stream function-vorticity form of the governing equations has been widely utilized.²⁵ In this form an efficient Gauss-Seidel relaxation algorithm is the natural choice of solution procedures. The non-primitive variables (stream function, ψ , and vorticity, ω) are defined as:²⁵

$$\frac{\partial \psi}{\partial r} = r \rho w \quad (\text{A1})$$

$$\frac{\partial \psi}{\partial z} = -r \rho u \quad (\text{A2})$$

$$\omega = \nabla \times \vec{V} = \left[\frac{\partial u}{\partial z} - \frac{\partial w}{\partial r} \right] = - \left[\frac{\partial}{\partial z} \left(\frac{1}{r \rho} \frac{\partial \psi}{\partial z} \right) + \frac{\partial}{\partial r} \left(\frac{1}{r \rho} \frac{\partial \psi}{\partial r} \right) \right] \quad (\text{A3})$$

The conservation equations for mass and momentum are given by:²⁵

$$\nabla \cdot \rho \vec{V} = \frac{\partial(r \rho u)}{\partial r} + \frac{\partial(r \rho w)}{\partial z} = 0 \quad (\text{A4})$$

$$\nabla \cdot [\rho u \vec{V} - \vec{\tau}_r] - \frac{1}{r} [\rho v^2 - \tau_{\theta\theta}] + \frac{\partial p}{\partial r} = 0 \quad (\text{A5})$$

$$\nabla \cdot [\rho w \vec{V} - \vec{\tau}_z] + \frac{\partial p}{\partial z} = 0 \quad (\text{A6})$$

$$\frac{1}{r} \nabla \cdot [r(\rho v \vec{V} - \vec{\tau}_\theta)] = 0 \quad (\text{A7})$$

The shear stress ($\vec{\tau}$) includes the Reynolds stress with an effective fluid viscosity expressed as the sum of molecular and turbulent viscosities.

Equation A4 is transformed into the non-primitive variables using Equations A1 and A2. The resulting equation demonstrates that the stream function, by definition, satisfies conservation of mass.

$$\frac{\partial}{\partial z} \left[\frac{\partial \psi}{\partial r} \right] - \frac{\partial}{\partial r} \left[\frac{\partial \psi}{\partial z} \right] = 0 \quad (\text{A8})$$

²⁵ Schlichting, H., *Boundary Layer Theory*, 7th ed., translated by J. Kestin, McGraw-Hill, New York, 1979.

Equations A5 and A6 are transformed into a single vorticity equation. First, the definition of ψ is used in these equations and yields:

$$-\frac{1}{r} \left[\frac{\partial}{\partial z} \left(\frac{1}{r\rho} \frac{\partial\psi}{\partial z} \frac{\partial\psi}{\partial r} \right) - \frac{\partial}{\partial r} \left(\frac{1}{r\rho} \frac{\partial\psi}{\partial z} \frac{\partial\psi}{\partial z} \right) \right] - \frac{1}{r} \rho v^2 = \nabla \cdot (\vec{\tau}_r) - \frac{1}{r} \tau_{\theta\theta} - \frac{\partial p}{\partial r} \quad (\text{A9})$$

$$\frac{1}{r} \left[\frac{\partial}{\partial z} \left(\frac{1}{r\rho} \frac{\partial\psi}{\partial r} \frac{\partial\psi}{\partial r} \right) - \frac{\partial}{\partial r} \left(\frac{1}{r\rho} \frac{\partial\psi}{\partial r} \frac{\partial\psi}{\partial z} \right) \right] = \nabla \cdot (\vec{\tau}_z) - \frac{\partial p}{\partial z} \quad (\text{A10})$$

The r -derivative of Equation A10 is subtracted from the z -derivative of Equation A9 and the definition of vorticity is introduced using Equation A3.

$$\begin{aligned} r\nabla \cdot \left[\frac{\omega}{r} \rho \vec{V} \right] &+ \frac{\partial\rho}{\partial z} \frac{\partial}{\partial r} \left[\frac{u^2 + w^2}{2} \right] - \frac{\partial\rho}{\partial r} \frac{\partial}{\partial z} \left[\frac{u^2 + w^2}{2} \right] - \frac{\partial}{\partial z} \left[\frac{1}{r} \rho v^2 \right] \\ &= \frac{\partial}{\partial z} \left[\frac{\partial}{\partial z} (\tau_{rz}) + \frac{1}{r} \frac{\partial}{\partial r} (r\tau_{rr}) \right] - \frac{\partial}{\partial r} \left[\frac{\partial}{\partial z} (\tau_{zz}) + \frac{1}{r} \frac{\partial}{\partial r} (r\tau_{zr}) \right] \\ &- \frac{\partial}{\partial z} \left(\frac{1}{r} \tau_{\theta\theta} \right) \end{aligned} \quad (\text{A11})$$

The right hand side of Equation A11 is expanded and the definition of vorticity (Equation A3) is again introduced to yield:

$$\begin{aligned} r\nabla \cdot \left[\frac{\omega}{r} \rho \vec{V} \right] &+ \frac{\partial\rho}{\partial z} \frac{\partial}{\partial r} \left[\frac{u^2 + w^2}{2} \right] - \frac{\partial\rho}{\partial r} \frac{\partial}{\partial z} \left[\frac{u^2 + w^2}{2} \right] - \frac{\partial}{\partial z} \left[\frac{1}{r} \rho v^2 \right] \\ &= \frac{1}{r^3} \nabla \cdot \left[r^2 \nabla \left(\frac{1}{r} \mu_{\text{eff}} \omega \right) \right] + S_\omega \end{aligned} \quad (\text{A12})$$

$$\begin{aligned} S_\omega &= \frac{2}{r} \nabla (\vec{V} \cdot \hat{z}) \cdot \left[\frac{\partial}{\partial z} (\nabla \mu_{\text{eff}} \cdot \hat{z}) \hat{r} - \frac{\partial}{\partial r} (\nabla \mu_{\text{eff}} \cdot \hat{z}) \hat{z} \right] \\ &+ \frac{2}{r} \nabla (\vec{V} \cdot \hat{r}) \cdot \left[\frac{\partial}{\partial z} (\nabla \mu_{\text{eff}} \cdot \hat{r}) \hat{r} - \frac{\partial}{\partial r} (\nabla \mu_{\text{eff}} \cdot \hat{r}) \hat{z} \right] \\ &- \frac{2}{r} \left[\frac{\partial}{\partial z} (\nabla \cdot \vec{V}) \hat{r} - \frac{\partial}{\partial r} (\nabla \cdot \vec{V}) \hat{z} \right] \cdot \nabla \mu_{\text{eff}} \end{aligned} \quad (\text{A13})$$

where,

$$\begin{aligned} \nabla A &= (\partial A / \partial r) \hat{r} + (\partial A / \partial z) \hat{z} \\ \hat{r} &= \text{unit vector in the } r\text{-direction} \\ \hat{z} &= \text{unit vector in the } z\text{-direction} \end{aligned}$$

Rearrangement and expansion of the gradient terms yields the final form of the vorticity equation:

$$\begin{aligned}
r^2 \left[\frac{\partial}{\partial z} \left(\frac{\omega}{r} \frac{\partial \psi}{\partial r} \right) - \frac{\partial}{\partial r} \left(\frac{\omega}{r} \frac{\partial \psi}{\partial z} \right) \right] &- \frac{\partial}{\partial z} \left[r^3 \frac{\partial}{\partial z} \left(\frac{\omega}{r} \mu_{\text{eff}} \right) \right] - \frac{\partial}{\partial r} \left[r^3 \frac{\partial}{\partial r} \left(\frac{\omega}{r} \mu_{\text{eff}} \right) \right] \\
&- r \frac{\partial}{\partial z} (\rho v^2) - r^2 \frac{\partial}{\partial z} \left(\frac{u^2 + w^2}{2} \right) \frac{\partial \rho}{\partial r} \\
&+ r^2 \frac{\partial}{\partial r} \left(\frac{u^2 + w^2}{2} \right) \frac{\partial \rho}{\partial z} - r^3 S_\omega = 0 \quad (\text{A14})
\end{aligned}$$

The azimuthal momentum equation (Equation A7) can be expressed in terms of the non-primitive variables as:

$$\frac{\partial}{\partial z} \left[r v \frac{\partial \psi}{\partial r} \right] - \frac{\partial}{\partial r} \left[r v \frac{\partial \psi}{\partial z} \right] - \frac{\partial}{\partial z} \left[r^3 \mu_{\text{eff}} \frac{\partial}{\partial z} \left(\frac{v}{r} \right) \right] - \frac{\partial}{\partial r} \left[r^3 \mu_{\text{eff}} \frac{\partial}{\partial r} \left(\frac{v}{r} \right) \right] = 0 \quad (\text{A15})$$

Energy conservation for a compressible flow is expressed by the First Law of Thermodynamics. The steady-state form of the First Law states that the net rate of stagnation enthalpy inflow for a control volume is equal to the sum of the shear work done by the contents of the control volume on the surroundings and the heat transfer to the surroundings.²⁵ Turbulence kinetic energy flux is also included in the balance, while radiation flux is neglected.

$$\nabla \cdot \left[\rho \vec{V} \tilde{h} + \vec{J}_h + \sum_j h_j \vec{J}_j + \vec{J}_k - (u \vec{\tau}_r + v \vec{\tau}_\theta + w \vec{\tau}_z) \right] = 0 \quad (\text{A16})$$

where,

\tilde{h} = the stagnation or total enthalpy of the mixture ($\tilde{h} = h + V^2/2$)

\vec{J}_h = $-(\Gamma_h)_{\text{eff}} c_p \nabla T$, the heat flux

Γ_h = thermal conductivity / specific heat of the mixture = μ_{eff} /Prandtl Number

c_p = $\sum_j c_{p,j} m_j$, the specific heat of the mixture at constant pressure

m_j = the mass fraction of species j

T = temperature

h_j = the heat of formation of species j

\vec{J}_j = $-(\Gamma_j)_{\text{eff}} \nabla m_j$, the mass flux of species j per unit area per unit time

Γ_j = mass diffusion coefficient \times mixture density = μ_{eff} /Schmidt Number

\vec{J}_k = $-(\Gamma_k)_{\text{eff}} \nabla k$, the flux of turbulence energy

Γ_k = turbulence kinetic energy diffusion coeff. \times mixture density = μ_{eff} /Schmidt Number

k = kinetic energy of the turbulent fluid motion ($V^2/2$ is the KE of the mean motion)

For turbulent flows, the subscript "eff", which stands for "effective", serves as a reminder that the turbulent fluid properties are being treated as kinematic properties with a set of augmented transport coefficients. The diffusion coefficients, Γ_h , Γ_j , and Γ_k are defined in terms of either the Prandtl Number ($c_p \mu / \kappa$) or the Schmidt Number ($\mu / (\rho D_j)$). These

nondimensional numbers represent the ratio of momentum transport to thermal conductivity (κ) and the ratio of viscous momentum transport to diffusive mass transport ($D_j =$ diffusion coefficient), respectively.

The energy equation, Equation A16, is transformed into stream function-vorticity form. First, the terms involving shear stress in Equation A16 can be expanded to yield:

$$u\vec{\tau}_r = \frac{1}{\mu_{\text{eff}}} [u\tau_{rr} + v\tau_{\theta r} + w\tau_{zr}] = \frac{\partial}{\partial r} \left(\frac{u^2 + v^2 + w^2}{2} \right) + \left[\frac{\partial}{\partial r} \left(\frac{u^2}{2} \right) - \frac{2}{3}u\nabla \cdot \vec{V} + w \frac{\partial u}{\partial z} - \frac{v^2}{r} \right] \quad (\text{A17})$$

$$v\vec{\tau}_\theta = \frac{1}{\mu_{\text{eff}}} [u\tau_{r\theta} + v\tau_{\theta\theta} + w\tau_{z\theta}] = \left[wr \frac{\partial}{\partial z} \left(\frac{v}{r} \right) + ur \frac{\partial}{\partial r} \left(\frac{v}{r} \right) + \frac{2uv}{r} - \frac{2}{3}v\nabla \cdot \vec{V} \right] \quad (\text{A18})$$

$$w\vec{\tau}_z = \frac{1}{\mu_{\text{eff}}} [u\tau_{rz} + v\tau_{\theta z} + w\tau_{zz}] = \frac{\partial}{\partial z} \left(\frac{u^2 + v^2 + w^2}{2} \right) + \left[\frac{\partial}{\partial z} \left(\frac{w^2}{2} \right) - \frac{2}{3}w\nabla \cdot \vec{V} + u \frac{\partial w}{\partial r} \right] \quad (\text{A19})$$

If the terms in square brackets of Equations A17-A19 are small and can be set to zero (which is exactly the case on a solid wall boundary), the shear stress term in Equation A16 can be more easily written as:

$$(u\vec{\tau}_r + v\vec{\tau}_\theta + w\vec{\tau}_z) = \mu_{\text{eff}} \nabla(V^2/2) = \mu_{\text{eff}} \nabla \left[\frac{u^2 + v^2 + w^2}{2} \right] \quad (\text{A20})$$

This assumption will significantly ease subsequent manipulations, and indeed Equation A20 serves as a good approximation for most practical applications.^{11,25} The equation for energy conservation is then given by:

$$\nabla \cdot \left[\rho \vec{V} \tilde{h} - (\Gamma_h)_{\text{eff}} c_p \nabla T - \sum_j h_j (\Gamma_j)_{\text{eff}} \nabla m_j - (\Gamma_k)_{\text{eff}} \nabla k - \mu_{\text{eff}} \nabla \left(\frac{V^2}{2} \right) \right] \simeq 0 \quad (\text{A21})$$

Equation A21 can be expressed in the non-primitive variables as:

$$\begin{aligned} & \frac{\partial}{\partial z} \left[\tilde{h} \frac{\partial \psi}{\partial r} \right] - \frac{\partial}{\partial r} \left[\tilde{h} \frac{\partial \psi}{\partial z} \right] - \frac{\partial}{\partial z} \left[(\Gamma_h)_{\text{eff}} r \frac{\partial \tilde{h}}{\partial z} \right] - \frac{\partial}{\partial r} \left[(\Gamma_h)_{\text{eff}} r \frac{\partial \tilde{h}}{\partial r} \right] - \\ & \frac{\partial}{\partial z} \left[\mu_{\text{eff}} r \left(\left(1 - \frac{1}{\sigma_h}\right) \frac{\partial(V^2/2)}{\partial z} + \left(\frac{1}{\sigma_k} - \frac{1}{\sigma_h}\right) \frac{\partial k}{\partial z} + \sum_j \left(\frac{1}{\sigma_j} - \frac{1}{\sigma_h}\right) h_j \frac{\partial m_j}{\partial z} \right) \right] - \\ & \frac{\partial}{\partial r} \left[\mu_{\text{eff}} r \left(\left(1 - \frac{1}{\sigma_h}\right) \frac{\partial(V^2/2)}{\partial r} + \left(\frac{1}{\sigma_k} - \frac{1}{\sigma_h}\right) \frac{\partial k}{\partial r} + \sum_j \left(\frac{1}{\sigma_j} - \frac{1}{\sigma_h}\right) h_j \frac{\partial m_j}{\partial r} \right) \right] \\ & \simeq 0 \end{aligned} \quad (\text{A22})$$

where,

$$\begin{aligned} \sigma_j &= \mu_{\text{eff}}/\Gamma_j, \text{ Schmidt Number} \\ \sigma_h &= \mu_{\text{eff}}/\Gamma_h, \text{ Prandtl Number} \\ \sigma_k &= \mu_{\text{eff}}/\Gamma_k, \text{ Schmidt Number} \end{aligned}$$

For a steady-state flow the conservation of chemical species states that the sum of the net inflow of species j by convection, the net inflow by diffusion, and the creation of species j by chemical reaction (R_j , per unit volume) within the control volume is equal to zero.

$$\frac{1}{r} \left[\frac{\partial}{\partial r} (r \rho u m_j + r J_{j,r}) + \frac{\partial}{\partial z} (r \rho w m_j + r J_{j,z}) \right] - R_j = 0 \quad (\text{A23})$$

Or in non-primitive variable form:

$$\frac{\partial}{\partial z} \left[m_j \frac{\partial \psi}{\partial r} \right] - \frac{\partial}{\partial r} \left[m_j \frac{\partial \psi}{\partial z} \right] - \frac{\partial}{\partial z} \left[(\Gamma_j)_{\text{eff}} r \frac{\partial m_j}{\partial z} \right] - \frac{\partial}{\partial r} \left[(\Gamma_j)_{\text{eff}} r \frac{\partial m_j}{\partial r} \right] - r R_j = 0 \quad (\text{A24})$$

The governing equations for stream-function (Equ. A3), vorticity (Equ. A14), azimuthal velocity (Equ. A15), stagnation enthalpy (Equ. A22) and species mass (Equ. A24) can be expressed in a general form as follows:

$$a_\phi \left[\frac{\partial}{\partial z} \left(\phi \frac{\partial \psi}{\partial r} \right) - \frac{\partial}{\partial r} \left(\phi \frac{\partial \psi}{\partial z} \right) \right] - \frac{\partial}{\partial z} \left[b_\phi r \frac{\partial}{\partial z} (c_\phi \phi) \right] - \frac{\partial}{\partial r} \left[b_\phi r \frac{\partial}{\partial r} (c_\phi \phi) \right] + r d_\phi = 0 \quad (\text{A25})$$

with,

$$\begin{aligned} \phi = \psi, & \quad a_\phi = 0, & \quad b_\phi = 1/(\rho r^2), & \quad c_\phi = 1, & \quad d_\phi = -\omega/r \\ \phi = \omega/r, & \quad a_\phi = r^2, & \quad b_\phi = r^2, & \quad c_\phi = \mu_{\text{eff}}, & \quad d_\phi = Q_\omega \\ \phi = rv, & \quad a_\phi = 1, & \quad b_\phi = \mu_{\text{eff}} r^2, & \quad c_\phi = 1/r^2, & \quad d_\phi = 0 \\ \phi = \tilde{h}, & \quad a_\phi = 1, & \quad b_\phi = (\Gamma_h)_{\text{eff}}, & \quad c_\phi = 1, & \quad d_\phi = Q_h - S_h \\ \phi = m_j, & \quad a_\phi = 1, & \quad b_\phi = (\Gamma_j)_{\text{eff}}, & \quad c_\phi = 1, & \quad d_\phi = -R_j \end{aligned}$$

where,

$$\begin{aligned} Q_\omega &= -\frac{\partial}{\partial z} (\rho v^2) - r \left[\frac{\partial}{\partial z} \left(\frac{u^2 + w^2}{2} \right) \frac{\partial \rho}{\partial r} - \frac{\partial}{\partial r} \left(\frac{u^2 + w^2}{2} \right) \frac{\partial \rho}{\partial z} \right] - r^2 S_\omega \\ Q_h &= \frac{1}{r} \frac{\partial}{\partial z} \left[\mu_{\text{eff}} r \left(\left(1 - \frac{1}{\sigma_h} \right) \frac{\partial (V^2/2)}{\partial z} + \left(\frac{1}{\sigma_k} - \frac{1}{\sigma_h} \right) \frac{\partial k}{\partial z} + \sum_j \left(\frac{1}{\sigma_j} - \frac{1}{\sigma_h} \right) h_j \frac{\partial m_j}{\partial z} \right) \right] \\ S_h &= \frac{1}{r} \frac{\partial}{\partial r} \left[\mu_{\text{eff}} r \left(\left(1 - \frac{1}{\sigma_h} \right) \frac{\partial (V^2/2)}{\partial r} + \left(\frac{1}{\sigma_k} - \frac{1}{\sigma_h} \right) \frac{\partial k}{\partial r} + \sum_j \left(\frac{1}{\sigma_j} - \frac{1}{\sigma_h} \right) h_j \frac{\partial m_j}{\partial r} \right) \right] \end{aligned}$$

The pressure can be recovered from the non-primitive variables after a converged solution of Equation A25 is achieved or after each iteration, if pressure variations are expected to have a significant effect on density. The radial and axial momentum equations (Equ. A5 and A6) can be rearranged to yield:

$$\frac{\partial p}{\partial z} = P_1(r, z) \quad \text{and} \quad \frac{\partial p}{\partial r} = P_2(r, z) \quad (\text{A26})$$

Then along any path from point A to point B in the flowfield, the pressure is given by:

$$p_B - p_A = \int_A^B (P_1 dz + P_2 dr) \quad (\text{A27})$$

Since p is a scalar, $p_B - p_A$ should be path independent and can serve as a consistency check on the converged solution. In most cases a pressure difference is desired to form the pressure coefficient at a point. However, if the pressure at point B is required, the pressure at point A is assigned to a known inlet pressure value, and integration proceeds from the inlet to point B .

A thermodynamic equation that relates the mixture density, ρ , and the mixture temperature, T , to the stagnation enthalpy, is given by,

$$d\tilde{h} = \sum_j (c_{pj} m_j) dT + \sum_j h_j dm_j + \frac{d(V^2)}{2} + dk \quad (\text{A28})$$

where, $d(V^2)/2$ and dk represent the kinetic energy from the mean flow and the fluctuating turbulent flow, respectively. The heats of formation, h_j , must be specified from a knowledge of the fuel chemistry. Assuming that h_j is evaluated at $T_o = 0$ and that the specific heats are independent of T (i.e. calorically perfect gases), then Equation A28 can be integrated to yield:

$$\tilde{h} = T \sum_j c_{pj} m_j + \sum_j h_j m_j + \frac{V^2}{2} + k \quad (\text{A29})$$

The calorically perfect gas assumption is made to ease the computational effort and is not unusual,¹² but it could be removed if the temperature dependence of c_p for the reactants and products were known. The temperature of the mixture is then expressed as:

$$T = \frac{\tilde{h} - \frac{V^2}{2} - k - \sum_j h_j m_j}{\sum_j c_{pj} m_j} \quad (\text{A30})$$

The specific volume of an individual species and the specific volume of the mixture are defined as:

$$U_j = \frac{\Re T}{p_j M_j} \quad (\text{A31})$$

$$U = U_j m_j = \frac{\Re T m_j}{p_j M_j} \quad (\text{A32})$$

where \Re is the universal gas constant and M_j is the molecular weight of species j (note, $U \neq \sum_j U_j m_j$ since all j components occupy the same volume). The mixture density is defined using $p = \sum_j p_j = \Re T \sum_j (m_j/M_j)/U$ and Equation A30.

$$\rho = \frac{1}{U} = \frac{p/\Re T}{\sum_j \frac{m_j}{M_j}} = \frac{p/\Re}{\tilde{h} - \frac{V^2}{2} - k - \sum_j h_j m_j} \cdot \frac{\sum_j c_{pj} m_j}{\sum_j \frac{m_j}{M_j}} \quad (\text{A33})$$

Appendix B

Finite difference formulae are employed to transform Equation A25 into an algebraic equation in ϕ for a single computational cell. The result for all cells in the computational mesh is a system of equations that can be solved efficiently using a Gauss-Seidel relaxation scheme. As outlined below, the computational stability of the scheme is insured since upwind differencing is employed for the convection terms. Under-relaxation is used to accelerate convergence and enhance stability when the magnitude of the source terms (especially with combustion) is large.

Figure B1 shows the computational mesh in the vicinity of a typical mesh point, P. The integration of Equation A25 is carried out on a rectangle with corner points denoted ne,se,sw,nw.

$$\begin{aligned} & \int_{r_s}^{r_n} \int_{z_w}^{z_e} a_\phi \left[\frac{\partial}{\partial z} \left(\phi \frac{\partial \psi}{\partial r} \right) - \frac{\partial}{\partial r} \left(\phi \frac{\partial \psi}{\partial z} \right) \right] dz dr - \\ & \int_{r_s}^{r_n} \int_{z_w}^{z_e} \left[\frac{\partial}{\partial z} \left(b_\phi r \frac{\partial}{\partial z} (c_\phi \phi) \right) + \frac{\partial}{\partial r} \left(b_\phi r \frac{\partial}{\partial r} (c_\phi \phi) \right) \right] dz dr + \\ & \int_{r_s}^{r_n} \int_{z_w}^{z_e} r d_\phi dz dr = 0 \end{aligned} \quad (\text{B1})$$

Equation B1 can be integrated if a_ϕ is constant which is the case for all ϕ except when $\phi = \omega/r$ (i.e. $a_\phi = r^2$). Assuming that $r_p^2 = r^2$ is a suitable average value for r^2 over the rectangle around point P, then Equation B1 is rewritten as:

$$\begin{aligned} & a_{\phi_P} \left[\int_{r_s}^{r_n} \left[\phi_e \left(\frac{\partial \psi}{\partial r} \right)_e - \phi_w \left(\frac{\partial \psi}{\partial r} \right)_w \right] dr - \int_{z_w}^{z_e} \left[\phi_n \left(\frac{\partial \psi}{\partial z} \right)_n - \phi_s \left(\frac{\partial \psi}{\partial z} \right)_s \right] dz \right] - \\ & \int_{r_s}^{r_n} \left[(rb_\phi)_e \left(\frac{\partial}{\partial z} (c_\phi \phi) \right)_e - (rb_\phi)_w \left(\frac{\partial}{\partial z} (c_\phi \phi) \right)_w \right] dr - \\ & \int_{z_w}^{z_e} \left[(rb_\phi)_n \left(\frac{\partial}{\partial r} (c_\phi \phi) \right)_n - (rb_\phi)_s \left(\frac{\partial}{\partial r} (c_\phi \phi) \right)_s \right] dz + \\ & \int_{r_s}^{r_n} \int_{z_w}^{z_e} r d_\phi dz dr = 0 \end{aligned} \quad (\text{B2})$$

where the subscripts n,e,s,w when applied to a spatial derivative indicate that the derivative is evaluated along the corresponding side of the rectangle. The terms in Equation B2 are due to convection, diffusion in the r -direction, diffusion in the z -direction and the source term, respectively. Each of these terms is treated in a separate way.

Consider the first integral for the convection terms in Equation B2:

$$I_c \equiv a_{\phi_P} \int_{r_s}^{r_n} \phi_e \left(\frac{\partial \psi}{\partial r} \right)_e dr \quad (\text{B3})$$

The average value for ϕ_e is defined by:

$$\bar{\phi}_e \equiv \frac{\int_{r_s}^{r_n} \phi \left(\frac{\partial \psi}{\partial r} \right)_e dr}{\int_{r_s}^{r_n} \left(\frac{\partial \psi}{\partial r} \right)_e dr} \simeq \frac{I_c}{[a_{\phi_P} (\psi_{ne} - \psi_{se})]} \quad (\text{B4})$$

such that the integral I_c is written as:

$$I_c = a_{\phi_P} \bar{\phi}_e (\psi_{ne} - \psi_{se}) \quad (B5)$$

The value of $\bar{\phi}_e$ is chosen as the value of ϕ "upwind" of the e-face of the rectangle. This is the upwind differencing method since the upwind direction depends upon the direction of the local velocity vector. Thus if $(\psi_{ne} - \psi_{se}) \simeq (\partial\psi/\partial r)_e > 0$ then $\bar{\phi}_e = \phi_P$ and if $(\psi_{ne} - \psi_{se}) \simeq (\partial\psi/\partial r)_e < 0$ then $\bar{\phi}_e = \phi_E$. Thus:

$$I_c \simeq a_{\phi_P} \phi_E [(\psi_{ne} - \psi_{se}) - |\psi_{ne} - \psi_{se}|]/2 + a_{\phi_P} \phi_P [(\psi_{ne} - \psi_{se}) + |\psi_{ne} - \psi_{se}|]/2 \quad (B6)$$

where the value of ψ at the rectangle corner points is a average of the values of ψ at the neighboring mesh points (i.e. $\psi_{se} \simeq [\psi_{SE} + \psi_E + \psi_P + \psi_S]/4$). Treating the other integrals of the convection terms in the same fashion we obtain:

$$I_{\text{convection}} \equiv A_E (\phi_P - \phi_E) + A_W (\phi_P - \phi_W) + A_N (\phi_P - \phi_N) + A_S (\phi_P - \phi_S) \quad (B7)$$

where,

$$\begin{aligned} A_E &\equiv a_{\phi_P} [(\psi_{se} - \psi_{ne}) + |\psi_{se} - \psi_{ne}|]/2 \\ A_W &\equiv a_{\phi_P} [(\psi_{nw} - \psi_{sw}) + |\psi_{nw} - \psi_{sw}|]/2 \\ A_N &\equiv a_{\phi_P} [(\psi_{ne} - \psi_{nw}) + |\psi_{ne} - \psi_{nw}|]/2 \\ A_S &\equiv a_{\phi_P} [(\psi_{sw} - \psi_{se}) + |\psi_{sw} - \psi_{se}|]/2 \end{aligned}$$

Note that the coefficients A_E , A_W , A_N , and A_S are positive or zero.

Consider the first integral for the diffusion terms in Equation B2:

$$I_d \equiv \int_{r_e}^{r_n} [rb_\phi]_e \left[\frac{\partial}{\partial z} (c_\phi \phi) \right]_e dr \quad (B8)$$

Assuming that $r_e \simeq (r_E + r_P)/2$, and that $b_{\phi_e} \simeq (b_{\phi_E} + b_{\phi_P})/2$ and using a central finite difference formula for $(\partial(c_\phi \phi)/\partial z)_e \simeq (c_{\phi_E} \phi_E - c_{\phi_P} \phi_P)/(z_E - z_P)$, then;

$$I_d = \left[\frac{b_{\phi_E} + b_{\phi_P}}{2} \right] \left[\frac{r_E + r_P}{2} \right] \left[\frac{c_{\phi_E} \phi_E - c_{\phi_P} \phi_P}{z_E - z_P} \right] \left[\frac{r_N - r_S}{2} \right] \quad (B9)$$

Treating the other integrals of the diffusion terms in the same fashion we obtain:

$$\begin{aligned} I_{\text{diffusion}} &= B_E [c_{\phi_E} \phi_E - c_{\phi_P} \phi_P] + B_W [c_{\phi_W} \phi_W - c_{\phi_P} \phi_P] + B_N [c_{\phi_N} \phi_N - c_{\phi_P} \phi_P] \\ &+ B_S [c_{\phi_S} \phi_S - c_{\phi_P} \phi_P] \end{aligned} \quad (B10)$$

where,

$$\begin{aligned} B_E &\equiv [(b_{\phi_E} + b_{\phi_P})/8][(r_N - r_S)/(z_E - z_P)][r_E + r_P] \\ B_W &\equiv [(b_{\phi_W} + b_{\phi_P})/8][(r_N - r_S)/(z_P - z_W)][r_W + r_P] \\ B_N &\equiv [(b_{\phi_N} + b_{\phi_P})/8][(z_E - z_W)/(r_N - r_P)][r_N + r_P] \\ B_S &\equiv [(b_{\phi_S} + b_{\phi_P})/8][(z_E - z_W)/(r_P - r_S)][r_S + r_P] \end{aligned}$$

Note that the coefficients B_E , B_W , B_N , and B_S are positive.

Consider the integral for the source term in Equation B2:

$$I_{\text{source}} \equiv \int_{r_s}^{r_n} \int_{z_w}^{z_e} r d_\phi dz dr = 0 \quad (\text{B11})$$

Assuming that d_ϕ is uniform over the area of integration (rectangle) and equal to d_P and that r_P is a close approximation to the space-averaged value of r over the area of integration then;

$$I_{\text{source}} \simeq d_{\phi_P} r_P \left[\frac{z_E - z_W}{2} \right] \left[\frac{r_N - r_S}{2} \right] \quad (\text{B12})$$

When the expression for d_ϕ involves spatial derivatives (e.g. when $\phi = \omega/r$ and $\phi = \tilde{h}$), central finite difference expressions are used. For example, $d_\phi = (\partial\phi/\partial r)_P$ is expressed on a non-uniform grid as:

$$\left(\frac{\partial\phi}{\partial r} \right)_P = \frac{(\phi_N - \phi_P)(r_P - r_S)/(r_N - r_P) + (\phi_P - \phi_S)(r_N - r_P)/(r_P - r_S)}{r_N - r_S} \quad (\text{B13})$$

which for a uniform grid reduces to $(\phi_N - \phi_S)/(r_N - r_S)$.

The complete finite difference form of Equation B2 for a single grid point is written as:

$$\begin{aligned} & A_E (\phi_P - \phi_E) + A_W (\phi_P - \phi_W) + A_N (\phi_P - \phi_N) + A_S (\phi_P - \phi_S) - \\ & B_E (c_{\phi_E} \phi_E - c_{\phi_P} \phi_P) - B_W (c_{\phi_W} \phi_W - c_{\phi_P} \phi_P) - \\ & B_N (c_{\phi_N} \phi_N - c_{\phi_P} \phi_P) - B_S (c_{\phi_S} \phi_S - c_{\phi_P} \phi_P) + d_{\phi_P} \Pi_P = 0 \end{aligned} \quad (\text{B14})$$

which is expressed as a successive-substitution formula by moving ϕ_P to the left-hand-side of Equation B14:

$$\phi_P = C_E \phi_E + C_W \phi_W + C_N \phi_N + C_S \phi_S + D \quad (\text{B15})$$

where,

$$\begin{aligned} C_E &= (A_E + B_E c_{\phi_E}) / \sum_{AB} \\ C_W &= (A_W + B_W c_{\phi_W}) / \sum_{AB} \\ C_N &= (A_N + B_N c_{\phi_N}) / \sum_{AB} \\ C_S &= (A_S + B_S c_{\phi_S}) / \sum_{AB} \\ D &= -d_{\phi_P} \Pi_P / \sum_{AB} \\ \sum_{AB} &= A_E + A_W + A_N + A_S + c_{\phi_P} (B_E + B_W + B_N + B_S) \\ A_E &= a_{\phi_P} [(\psi_{SE} + \psi_S - \psi_{NE} - \psi_N) + |\psi_{SE} + \psi_S - \psi_{NE} - \psi_N|] / 8 \\ A_W &= a_{\phi_P} [(\psi_{NW} + \psi_N - \psi_{SW} - \psi_S) + |\psi_{NW} + \psi_N - \psi_{SW} - \psi_S|] / 8 \\ A_N &= a_{\phi_P} [(\psi_{NE} + \psi_E - \psi_{NW} - \psi_W) + |\psi_{NE} + \psi_E - \psi_{NW} - \psi_W|] / 8 \\ A_S &= a_{\phi_P} [(\psi_{SW} + \psi_W - \psi_{SE} - \psi_E) + |\psi_{SW} + \psi_W - \psi_{SE} - \psi_E|] / 8 \\ \Pi_P &= r_P (z_E - z_W)(r_N - r_S) / 4 \\ B_E &= [(b_{\phi_E} + b_{\phi_P}) / 8] [(r_N - r_S) / (z_E - z_P)] [r_E + r_P] \\ B_W &= [(b_{\phi_W} + b_{\phi_P}) / 8] [(r_N - r_S) / (z_P - z_W)] [r_W + r_P] \\ B_N &= [(b_{\phi_N} + b_{\phi_P}) / 8] [(z_E - z_W) / (r_N - r_P)] [r_N + r_P] \\ B_S &= [(b_{\phi_S} + b_{\phi_P}) / 8] [(z_E - z_W) / (r_P - r_S)] [r_S + r_P] \end{aligned}$$

Equation B15 represents a successive-substitution formula for ϕ_P at each grid point on the computational mesh. The resulting system of equations for the entire mesh is solved using a Gauss-Seidel relaxation scheme. Each iteration cycle is made up of N sub-cycles, where N is the number of equations (see Equation A25) being considered (N must be at least 2 since the equations for $\phi = \omega/r$ and $\phi = \psi$ are the minimum required to define the flow). In each sub-cycle, each grid point is scanned row by row and a single variable is updated using Equation B15. The variables ω/r and ψ are updated in order, followed by all other variables. When all sub-cycles are completed, a new iteration cycle is started in which the values of the variables from the latest iteration are immediately used. This is consistent with the Gauss-Seidel methodology.²⁵ This procedure is repeated until convergence is achieved. Convergence is usually indicated by satisfaction of one or both of the following criteria:

$$\left[\frac{\phi^{(k)} - \phi^{(k-1)}}{\phi^{(k)}} \right]_{\max} \leq \lambda_1 \quad (\text{B16})$$

$$\left[\frac{\phi^{(k)} - \phi^{(k-1)}}{\phi_{\max}^{(k-1)}} \right]_{\max} \leq \lambda_2 \quad (\text{B17})$$

where λ_1 and λ_2 are small ($\lambda_1 \leq .005$ and $\lambda_2 \leq \lambda_1/100$) and superscript k represents values at the latest iteration cycle.

For the successive-substitution formula (Equation B15) to be stable and convergent, three criteria must be met.²⁶

1. The sum of the moduli of C_E , C_W , C_N , and C_S must be less than or equal to 1 at every grid point.
2. The sum of the moduli of C_E , C_W , C_N , and C_S must be less than 1 for at least one grid point.
3. The coefficients (C and D) of ϕ in Equation B15 must not vary greatly from one cycle to the next.

The coefficients, C , are comprised of coefficients, A and B , which are greater than zero (a direct consequence of upwind differencing used for the convection terms, see Appendix B). This implies that the C coefficients are greater than zero and that $\sum C = 1$ provided the c_ϕ coefficients are equal. In fact $c_\phi = 1$ for all definitions of ϕ except when $\phi = \omega/r$ and $\phi = rv$ (Equation A25). However, the relaxation scheme may be stable and converge if the variation in c_ϕ between neighboring grid points is small and thus $\sum C \approx 1$. Item 1 of the stability criteria will, therefore, be satisfied.

Along the boundary of the computational domain, there will be at least one case where $\phi_P = \text{constant}$. Thus the C coefficients of Equation B15 will be zero and so $\sum C < 1$ for the grid points along the boundary. Item 2 of the stability criteria will, therefore, be satisfied.

Satisfaction of the third criteria cannot be shown formally. The computational grid must be appropriately defined with clustering in regions of large ϕ gradients. The initial and boundary conditions must be consistent with the mathematical nature of the governing

²⁶ Carnahan, B., Luther, H.A., and Wilkes, J.O., *Applied Numerical Methods*, John Wiley and Sons, New York, 1969.

partial differential equations. In addition, the variation in the source terms must not be stronger than the damping of the viscous terms in the equations. If divergence is found to occur, then under-relaxation techniques can be employed to stabilize the iteration scheme. In contrast, over-relaxation techniques tend to accelerate the convergence of a stable scheme, but they are not recommended for equations with strong source terms. Under-relaxation is defined for iteration number k by $\phi^{(k)} = a_{ur}\phi^{(k)} + (1 - a_{ur})\phi^{(k-1)}$, where $0 < a_{ur} < 1$ and $a_{ur} = 1$ for no under-relaxation. For the current governing equations and combustion model, under-relaxation was not required for convergence to a stable solution.

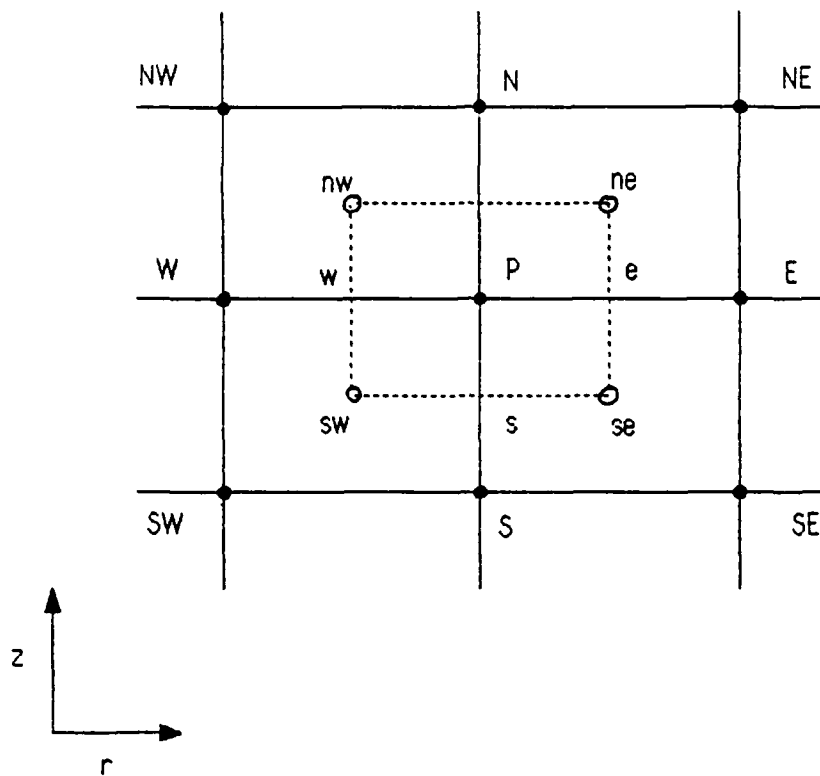


Figure B1. Portion of the Computational Grid. Solid circles are grid points. Open circles are cell centroids. Dotted lines enclose the rectangular area of integration.

List of Symbols

a_{ur}	under-relaxation factor
c_p	specific heat at constant pressure
C_D	drag coefficient (Equation 15)
D	maximum diameter of the combustion chamber
f	mixture fraction (Equations 5-7)
g	acceleration due to gravity
h	heat of formation
h_v	heat of vaporization
\tilde{h}	total enthalpy (Equation A29)
J	flow rate or flux
k	turbulence kinetic energy
L	length of the combustion chamber
m	mass fraction
M	molecular weight
n	stoichiometric air/fuel mass ratio
\hat{n}	unit vector in the normal direction
p	static pressure
Pr	Prandtl Number (see also σ_h)
q	heat flux
\mathcal{R}	universal gas constant
r	radial direction
\dot{r}	solid fuel regression rate (Equation 12)
R	reaction rate per unit volume
Re	Reynolds Number
S	area
Sc	Schmidt Number (see also σ_j and σ_k)
t	time
t_{fu}	thickness of the solid fuel layer
T	temperature (Equation A30)
u	velocity component in the axial direction
v	velocity component in the azimuthal direction (swirl velocity)
V	magnitude of the local velocity vector
\vec{V}	$u\hat{r} + v\hat{\theta} + w\hat{z}$
w	velocity component in the radial direction
z	axial direction

Greek Symbols

Γ	diffusion coefficient
ϵ	turbulence dissipation rate
θ	azimuthal direction
κ	thermal conductivity
μ	molecular viscosity (Equation 10-11)
ρ	density (Equation A33)

σ_h	$\mu_{\text{eff}}/\Gamma_h$, Prandtl Number
σ_j	$\mu_{\text{eff}}/\Gamma_j$, Schmidt Number
σ_k	$\mu_{\text{eff}}/\Gamma_k$, Schmidt Number
τ	shear stress
ϕ	general flow variable (Equation A25)
ψ	stream function (Equation A1-A2)
ω	vorticity (Equation A3)
U	specific volume (Equation A31-A32)

Superscripts

$\hat{\quad}$	unit vector
\sim	total or stagnation
\cdot	rate

Subscripts

eff	effective
fo	fuel-oxidizer
fp	fuel-products
fu	fuel
h	enthalpy
j	j -th mixture component
k	turbulence kinetic energy
op	oxidizer-products
ox	oxidizer
p	constant pressure
pr	products
r	radial component
ref	reference
st	stoichiometric
t	turbulent
vap	vaporization
wall	on the wall
z	axial component
θ	azimuthal component

DISTRIBUTION LIST

<u>No. of Copies</u>	<u>Organization</u>	<u>No. of Copies</u>	<u>Organization</u>
12	Administrator Defense Technical Info Center ATTN: DTIC-DDA Cameron Station Alexandria, VA 22304-6145	1	Director Benet Weapons Laboratory Armament RD&E Center US Army AMCCOM ATTN: SMCAR-LCB-TL Watervliet, NY 12189-4050
1	HQDA (SARD-TR) Washington, DC 20310-0001	1	Commander US Army Armament, Munitions and Chemical Command ATTN: SMCAR-ESP-L Rock Island, IL 61299-5000
1	Commander US Army Materiel Command ATTN: AMCDRA-ST 5001 Eisenhower Avenue Alexandria, VA 22333-0001	1	Commander US Army Aviation Systems Command ATTN: AMSAV-DACL 4300 Goodfellow Blvd. St. Louis, MO 63120-1798
1	Commander US Army Laboratory Command ATTN: AMSLC-DL Adelphi, MD 20783-1145	1	Director US Army Aviation Research and Technology Activity Ames Research Center Moffett Field, CA 94035-1099
2	Commander Armament RD&E Center US Army AMCCOM ATTN: SMCAR-MSI Picatinny Arsenal, NJ 07806-5000	1	Commander US Army Communications - Electronics Command ATTN: AMSEL-ED Fort Monmouth, NJ 07703-5022
2	Commander Armament RD&E Center US Army AMCCOM ATTN: SMCAR-TDC Picatinny Arsenal, NJ 07806-5000	1	Commander US Army Missile Command ATTN: AMSMI-RD Redstone Arsenal, AL 35898-5000
1	Commander Armament RD&E Center US Army AMCCOM ATTN: SMCAR-AER-A (R. Kline) Picatinny Arsenal, NJ 07806-5000	1	Commander US Army Missile Command ATTN: AMSMI-AS Redstone Arsenal, AL 35898-5010
2	Commander Armament RD&E Center US Army AMCCOM ATTN: SMCAR-FSP-A (F. Scerbo) (J. Bera) Picatinny Arsenal, NJ 07806-5000	1	Commander US Army Tank Automotive Command ATTN: ASQNC-TAC-DI (Technical Library) Warren, MI 48397-5000

DISTRIBUTION LIST

<u>No. of Copies</u>	<u>Organization</u>	<u>No. of Copies</u>	<u>Organization</u>
1	Director US Army TRADOC Analysis Command ATTN: ATAA-SL White Sands Missile Range NM 88002-5502	1	Director National Aeronautics and Space Administration Langley Research Center ATTN: Technical Library Langley Station Hampton, VA 23365
1	Commandant US Army Infantry School ATTN: ATSH-CD-CSO-OR Fort Benning, GA 31905-5660	1	Director National Aeronautics and Space Administration Marshall Space Flight Center ATTN: Dr. W.W. Fowlis Huntsville, AL 35812
1	AFWL/SUL Kirtland AFB, NM 87117-5800	1	Director National Aeronautics and Space Administration Ames Research Center ATTN: Dr. J. Steger Moffett Field, CA 94035
1	Air Force Armament Laboratory ATTN: AFATL/DLODL Eglin AFB, FL 32542-5000	1	Aerospace Corporation Aero-Engineering Subdivision ATTN: Walter F. Reddall El Segundo, CA 90245
1	Commander Naval Surface Weapons Center ATTN: Dr. W. Yanta Aerodynamics Branch K-24, Bldg. 402-12 White Oak Laboratory Silver Spring, MD 20910	1	Calspan Corporation ATTN: W. Rae P.O. Box 400 Buffalo, NY 14225
1	Commander Defense Advanced Research Projects Agency ATTN: MAJ R. Lundberg 1400 Wilson Blvd. Arlington, VA 22209	1	Hughes Aircraft ATTN: Dr. John McIntyre Mail Code S41/B323 P.O. Box 92919 Los Angeles, CA 90009
1	Director Lawrence Livermore National Laboratory ATTN: Mail Code L-35 (Mr. T. Morgan) P.O. Box 808 Livermore, CA 94550	1	Interferometrics, Inc. ATTN: Mr. R.F. L'Arriva 8150 Leesburg Pike Vienna, VA 22180
2	Director Sandia National Laboratories ATTN: Dr. W. Oberkamp Dr. W.P. Wolfe Division 1636 Albuquerque, NM 87185	2	United Technologies Corporation Chemical Systems Division ATTN: Dr. R.O. MacLaren Mr. A.L. Holzman 600 Metcalf Road, P.O. Box 50015 San Jose, CA 95150-0015

DISTRIBUTION LIST

<u>No. of Copies</u>	<u>Organization</u>	<u>No. of Copies</u>	<u>Organization</u>
3	Rockwell International Science Center ATTN: Dr. V. Shankar Dr. S. Chakravarthy Dr. S. Palaniswamy 1049 Camino Dos Rios P.O. Box 1085 Thousand Oaks, CA 91360	1	University of Colorado Department of Astro-Geophysics ATTN: E.R. Benton Boulder, CO 80302
1	Arizona State University Department of Mechanical and Energy Systems Engineering ATTN: Dr. G.P. Neitzel Tempe, AZ 85281	1	University of Delaware Spencer Laboratory Department of Mechanical Engineering ATTN: Prof. Leonard W. Schwartz Newark, DE 19716
1	Director Johns Hopkins University Applied Physics Laboratory ATTN: Dr. Fred Billig Johns Hopkins Road Laurel, MD 20707	2	University of Maryland ATTN: W. Melnik J.D. Anderson College Park, MD 20740
1	Massachusetts Institute of Technology ATTN: H. Greenspan 77 Massachusetts Avenue Cambridge, MA 02139	1	University of Maryland Baltimore County Department of Mathematics ATTN: Dr. Y.M. Lynn 5401 Wilkens Avenue Baltimore, MD 21228
1	North Carolina State University Mechanical and Aerospace Engineering Department ATTN: F.F. DeJarnette Raleigh, NC 27607		<u>Aberdeen Proving Ground</u> Director, USAMSAA ATTN: AMXSY-D AMXSY-MP, H. Cohen
1	Northwestern University Department of Engineering Science and Applied Mathematics ATTN: Dr. S.H. Davis Evanston, IL 60201		Commander, USATECOM ATTN: AMSTE-TO-F
1	Renssalaer Polytechnic Institute Department of Math Sciences Troy, NY 12181		Commander, CRDEC, AMCCOM ATTN: SMCCR-RSP-A M.C. Miller D. Olsen SMCCR-MU W. Dee C. Hughes D. Bromley SMCCR-SPS-IL
1	University of California - Davis ATTN: Dr. Harry A. Dwyer Davis, CA 95616		

USER EVALUATION SHEET/CHANGE OF ADDRESS

This laboratory undertakes a continuing effort to improve the quality of the reports it publishes. Your comments/answers below will aid us in our efforts.

1. Does this report satisfy a need? (Comment on purpose, related project, or other area of interest for which the report will be used.) _____

2. How, specifically, is the report being used? (Information source, design data, procedure, source of ideas, etc.) _____

3. Has the information in this report led to any quantitative savings as far as man-hours or dollars saved, operating costs avoided, or efficiencies achieved, etc? If so, please elaborate. _____

4. General Comments. What do you think should be changed to improve future reports? (Indicate changes to organization, technical content, format, etc.) _____

BRL Report Number _____ Division Symbol _____

Check here if desire to be removed from distribution list. _____

Check here for address change. _____

Current address: Organization _____
Address _____

-----FOLD AND TAPE CLOSED-----

Director
U.S. Army Ballistic Research Laboratory
ATTN: SLCBR-DD-T(NEI)
Aberdeen Proving Ground, MD 21005-5066

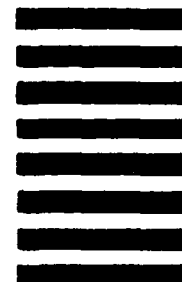


NO POSTAGE
NECESSARY
IF MAILED
IN THE
UNITED STATES

OFFICIAL BUSINESS
PENALTY FOR PRIVATE USE \$300

BUSINESS REPLY LABEL
FIRST CLASS PERMIT NO. 12062 WASHINGTON D. C.

POSTAGE WILL BE PAID BY DEPARTMENT OF THE ARMY



Director
U.S. Army Ballistic Research Laboratory
ATTN: SLCBR-DD-T(NEI)
Aberdeen Proving Ground, MD 21005-9989